J. Fluid Mech. (2021), vol. 919, A24, doi:10.1017/jfm.2021.395

Three-dimensional structural characteristics of flow separation induced by a forward-facing step in a turbulent channel flow

Xingjun Fang[1],†, **Mark F. Tachie**[1], **Donald J. Bergstrom**[2], **Zixuan Yang**[3] **and Bing-Chen Wang**[1]

[1]Department of Mechanical Engineering, University of Manitoba, Winnipeg, MB R3T 5V6, Canada

[2]Department of Mechanical Engineering, University of Saskatchewan, Saskatoon, SK S7N 5A9, Canada

[3]Institute of Mechanics, Chinese Academy of Sciences, Beijing 100190, PR China

(Received 18 July 2020; revised 23 April 2021; accepted 29 April 2021)

Separating and reattaching turbulent flows induced by a forward-facing step subjected to an incoming fully developed turbulent channel flow are studied using direct numerical simulation. The step height is one quarter of the channel height, and the Reynolds number based on friction velocity and half-channel height at the inlet is 180. The three-dimensional spatio-temporal characteristics of separation bubbles upstream and downstream of the step are analysed with particular attention to the effects of impinging hairpin structures and the topology of principal stretching. Immediately upstream of the step, the fluctuating vorticity parallel to the mean streamlines is significant. On the frontal surface of the step, strong spanwise skin friction appears in the form of alternating positive and negative values in vertical strips. Over the step, the principal stretching switches orientation along a curve emanating from the leading edge, which is termed the principal stretching line (PSL). The reverse flows upstream and downstream of the step possess dominant and harmonic frequencies that mirror those of the incoming flow. As a hairpin structure leans over the step, the associated vorticity is deformed by the principal stretching. Specifically, PSL marks the lower bound of the deformed hairpin legs, and an opposite-signed pair of counter-rotating quasi-streamwise vortices are induced near the top surface of the step. Consequently, the separation bubbles upstream of and over the step are enlarged and suppressed, respectively. For a sufficiently strong hairpin structure interacting with the step, an open-type separation occurs upstream of the step, while dual separation bubbles appear over the step.

Key words: boundary layer separation, turbulent boundary layers

---

† Email address for correspondence: fangx@myumanitoba.ca

1. Introduction

Separating and reattaching flows have been investigated extensively due to their important role in the transport of heat, mass and momentum in a broad range of engineering and industrial applications, such as heat exchangers, combustion chambers and polymer processing devices (Chiba, Ishida & Nakamura 1995; Abu-Mulaweh, Armaly & Chen 1996). For example, a sudden contraction of a flow channel in the form of a forward-facing step (FFS) induces flow separation, which in turn can cause a variety of favourable or undesirable effects including increased drag, acoustic noise and heat transfer as well as flow-induced structure vibration.

Considerable research has been performed over the past three decades to understand the three-dimensional (3-D) flow topology induced by an FFS with upstream laminar channel flows (Stüer, Gyr & Kinzelbach 1999; Wilhelm, Härtel & Kleiser 2003; Marino & Luchini 2009; Lanzerstorfer & Kuhlmann 2012). By employing the hydrogen-bubble visualization technique and particle tracking velocimetry, Stüer *et al.* (1999) observed that the laminar separation bubble upstream of an FFS is persistently three dimensional, and the fluid entrained into the separation bubble is released over the step in the form of streamwise-elongated streaks that are quasi-periodic in the spanwise direction. Wilhelm *et al.* (2003) performed linear stability analysis and direct numerical simulation (DNS) for fully developed laminar channel flow over an FFS. They observed that even though the flow is not absolutely unstable, weak oncoming perturbations can trigger a 3-D state in the separation bubble upstream of the step, which manifests itself as the 3-D topological streamlines observed by Stüer *et al.* (1999). Such sensitivity of the separation bubble upstream of the step to the incoming perturbation was also observed in subsequent numerical studies by Marino & Luchini (2009) and Lanzerstorfer & Kuhlmann (2012).

Turbulent flows over an FFS have been extensively investigated in terms of the effects of Reynolds number, relative step height (δ/h, where δ and h are the upstream boundary layer thickness and step height, respectively) and wall roughness on the statistics of turbulence and wall pressure (Camussi *et al.* 2008; Hattori & Nagano 2010; Sherry, Lo Jacono & Sheridan 2010; Ren & Wu 2011). Recent investigations of turbulent flows over FFS have focused on the unsteadiness of the separation bubbles (Pearson, Goulart & Ganapathisubramani 2013; Graziani *et al.* 2018; Fang & Tachie 2020). These experimental studies were performed using either planar time-resolved particle image velocimetry (TR-PIV) (Pearson *et al.* 2013; Fang & Tachie 2020) or double-frame planar PIV in conjunction with time-resolved wall pressure measurements (Graziani *et al.* 2018). In Graziani *et al.* (2018) the time-resolved velocity field in the streamwise-vertical plane was reconstructed using linear stochastic estimation (Adrian & Moin 1988) based on the low-repetition measurement of the velocity field and time-resolved measurement of the wall pressure. The main focus of Pearson *et al.* (2013) was to investigate the effects of the incoming turbulent boundary layer (TBL) on the unsteadiness of the separation bubble in front of the FFS. They observed that the low-velocity region of the incoming streaky structure, in the form of either large-scale motion (LSM) (Adrian, Meinhart & Tomkins 2000) or superstructure (Ganapathisubramani, Clemens & Dolling 2007), induces an enlarged separation bubble upstream of the step and, consequently, the separation bubble exhibits a flapping motion at the characteristic frequency of the incoming streaky structure. Graziani *et al.* (2018), who measured the separation bubbles upstream of and over the step concurrently, observed that both separation bubbles possess a low-frequency flapping motion, and are generally out of phase, i.e. an enlarged separation bubble upstream of the step typically corresponds to a contracted separation bubble over the step. By analysing the probability density function of the instantaneous reverse flow area, Graziani *et al.* (2018)

concluded that the non-existence or massive upstream separation bubble is less probable in their experiment compared with Pearson *et al.* (2013). Graziani *et al.* (2018) attributed these distinctions to the specific characteristics of the oncoming flow, i.e. their oncoming TBL is thin ($\delta/h = 0.49$) as opposed to the thicker oncoming TBL ($\delta/h = 1.47$) in Pearson *et al.* (2013). Most recently, Fang & Tachie (2020) studied the unsteadiness of separation bubbles upstream of and over an FFS submerged in a thick TBL ($\delta/h = 6.5$) using a TR-PIV system. They observed that the separation bubble over the step possesses a flapping motion at a frequency identical to the characteristic frequency of the LSM in the oncoming TBL, and exhibits a higher frequency oscillation when the separation bubble upstream of the step is enlarged.

Even though these time-resolved planar measurements provide important insight into the spatio-temporal characteristics of separation bubbles induced by an FFS subject to incoming turbulent flows (Pearson *et al.* 2013; Graziani *et al.* 2018; Fang & Tachie 2019*b*, 2020), little is known about the pertinent 3-D characteristics. Alam & Sandham (2000) compared the two-dimensional (2-D) and 3-D DNS of flow separations induced by an adverse pressure gradient with oncoming laminar flow, and concluded that the 2-D simulation cannot represent adequately the characteristics of the separation bubble. Complete 3-D information of turbulent separations induced by an FFS is useful to supplement the knowledge of the unsteadiness of flow separation in the streamwise-vertical plane accumulated by Pearson *et al.* (2013), Graziani *et al.* (2018), Fang & Tachie (2019*b*) and Fang & Tachie (2020). Therefore, we perform a DNS study of turbulent separations induced by an FFS in a fully developed turbulent channel flow. The goals are to provide detailed analysis of the 3-D spatio-temporal characteristics of the separation bubbles upstream and downstream of a step, with particular attention to the interaction of incoming turbulence structures with the step.

The remainder of this paper is organized as follows. In § 2 the numerical set-up, including the numerical algorithm, computational domain, boundary conditions and grid verification, are detailed. In § 3 the results are analysed in terms of the mean flow field, turbulence statistics, two-point correlations, 3-D spatio-temporal characteristics of turbulent separations, as well as the interaction between an idealized hairpin vortex and the step. Finally, § 4 summarizes the major conclusions of the present research.

2. Numerical set-up

2.1. *Numerical algorithm*

The continuity and Navier–Stokes (N–S) equations for incompressible flow are, respectively, written as

$$\frac{\partial u_i}{\partial x_i} = 0 \tag{2.1}$$

and

$$\frac{\partial u_i}{\partial t} + u_j \frac{\partial u_i}{\partial x_j} = -\frac{1}{\rho}\frac{\partial p}{\partial x_i} + \nu \frac{\partial^2 u_i}{\partial x_j^2} + f_i. \tag{2.2}$$

In the above equations, t, ρ, ν and p are time, density, kinematic viscosity and pressure, respectively; u_i and f_i represent the velocity and body force (such as streamwise pressure gradient) in the x_i (with $i = 1$, 2 and 3) direction, respectively. For convenience, we also use u, v and w to denote u_1, u_2 and u_3, respectively, and use x, y and z to denote x_1, x_2 and x_3, respectively.

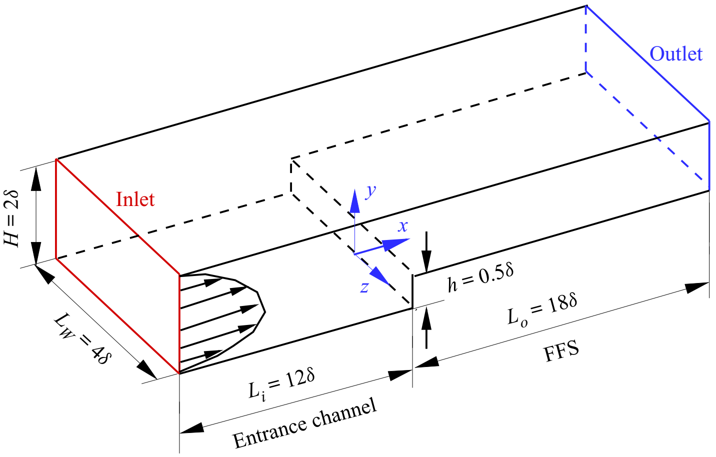

Figure 1. Schematic of the computational domain (not to scale) and the coordinate system.

An open-source code (named 'Semtex') publicly shared by Blackburn & Sherwin (2004) under the GNU general public license is modified for the present DNS study. This code implements the spectral-element-Fourier method (Blackburn *et al.* 2019) using C/C++ and FORTRAN languages, and is parallelized under the message passing interface standard. All variables are expressed in the functional space spanned by Gauss–Lobatto–Legendre Lagrange interpolants in the x–y plane and Fourier series in the z direction. The high-order time splitting method (Karniadakis, Israeli & Orszag 1991) is employed for time integration. An in-depth description of the spectral-element-Fourier algorithm is available in Blackburn *et al.* (2019) and Fang (2017).

2.2. *Flow configuration*

Figure 1 shows a schematic of the computational domain and the coordinate system used in this paper. The test geometry consists of an entrance channel of height $H = 2\delta$ and length $L_i = 12\delta$ followed by an FFS of height $h = 0.5\delta$ and length $L_o = 18\delta$, where δ denotes the half-channel height at the inlet. The blockage ratio (h/H) of the FFS is 25 %, i.e. $h = 0.25H$, and the spanwise width of the computational domain (L_W) is 4δ. The origin of the coordinate system is positioned at the bottom edge of the FFS in the mid-span.

The zero-velocity boundary condition is applied on the top and bottom surfaces of the computational domain, as well as the frontal and top surfaces of the FFS. A periodic boundary condition is used in the spanwise direction, while a convective boundary condition is implemented at the outlet. To provide a realistic turbulent flow upstream of the FFS, the unsteady velocity field at the inlet plane is extracted from a cross-stream plane in a simultaneously running DNS of fully developed turbulent channel flow at $Re_\tau \equiv U_\tau\delta/\nu = 180$, where U_τ is the friction velocity. The DNS of fully developed turbulent channel flow uses the same computational domain and grid as the entrance channel in figure 1, which is $12\delta \times 2\delta \times 4\delta$ in the streamwise, vertical and spanwise directions, respectively. This computational domain is similar to that $(4\pi\delta \times 2\delta \times 4\pi\delta/3)$ used in the database generated by Moser, Kim & Mansour (1999). The spanwise width of the computational domain was also examined by using the two-point autocorrelation and energy spectra, to ensure that the spanwise wavelength beyond L_W is of negligible significance.

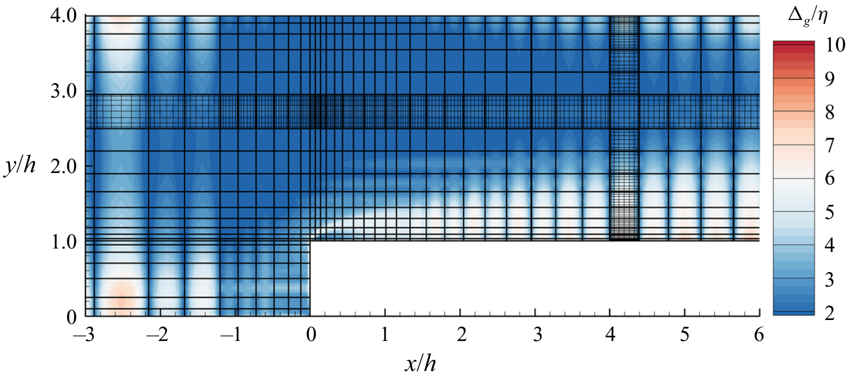

Figure 2. Distribution of the spectral elements and contours of the ratio between grid size ($\Delta_g \equiv \max(\Delta x, \Delta y, \Delta z)$) and Kolmogorov length scale (η) near the FFS. Collocation points within representative spectral elements are shown for illustration.

To discretize the computational domain shown in figure 1, rectangular (orthogonal) elements in conjunction with eighth-order Gauss–Lobatto–Legendre (GLL) nodes are used in the x–y plane, whereas uniformly distributed grids are employed in the z direction. Figure 2 shows representative elements near the FFS in the x–y plane. Note that the GLL nodes are more clustered towards the edge of elements. The streamwise lengths of the elements for $x/\delta \in [-12.0, -1.44]$ are constant at 0.48δ, which corresponds to a maximum streamwise grid spacing of $\Delta x^+_{max} = 15.4$, where the superscript $(\cdot)^+$ represents wall units. This value is smaller than that (17.7) used by Moser *et al.* (1999). In the vertical direction 22 elements are used for $y/\delta \in [0, 2]$, where 7 elements are below the step height (i.e. $y/\delta \in [0, 0.5]$). As such, $\Delta y^+ = 0.4$ on the top and bottom walls, whereas $\Delta y^+ = 0.1$ on the top surface of the FFS. In the spanwise direction 240 uniformly distributed grids were used. This corresponds to $\Delta z^+ = 3$, which value is almost half of that used by Moser *et al.* (1999). Figure 3 compares the flow statistics near the inlet at $x/\delta = -11.76$ with the database of Moser *et al.* (1999). This streamwise location is at the streamwise centre of the first layer of elements at the inlet, so that it represents the 'worst' grid resolution in the computational domain to resolve the fully developed turbulent channel flow. From figure 3, the turbulence statistics at the inlet are in good agreement with those from Moser *et al.* (1999). The distribution of elements away from the inlet are designed so that the ratio between grid size ($\Delta_g \equiv \max(\Delta x, \Delta y, \Delta z)$) and the Kolmogorov length scale ($\eta \equiv \nu^{3/4}\varepsilon^{-1/4}$, where $\varepsilon \equiv \nu\overline{(\partial u_i'/\partial x_j)^2}$ is the viscous dissipation rate for turbulence kinetic energy) is smaller than the maximum value ($(\Delta_g/\eta)_{max} \approx 10$ occurring at $x/\delta = -11.76$) near the inlet. In fact, it is seen from figure 2 that the levels of Δ_g/η near the FFS are all below 7. In total, 25×10^6 independent grid points were used. It is also worth mentioning that the lack (if any) of spatial resolution would manifest as a spiky distribution of the dissipation rate at the interfaces between elements. This is because if grid independence is not achieved, the calculated dissipation rate, which is sensitive to small-scale motions, would reflect the non-uniformity of the grid within the elements. We did not see any non-physical spiky distribution of dissipation rate over the entire computational domain (see figure 3*c* for example). Overall, the present spatial resolution is sufficient.

The time step was fixed at $\Delta t = 0.0003\delta/U_C$, where U_C is the streamwise mean velocity at the central height ($y/\delta = 1$) of the inlet, as such the Courant–Friedrichs–Lewy

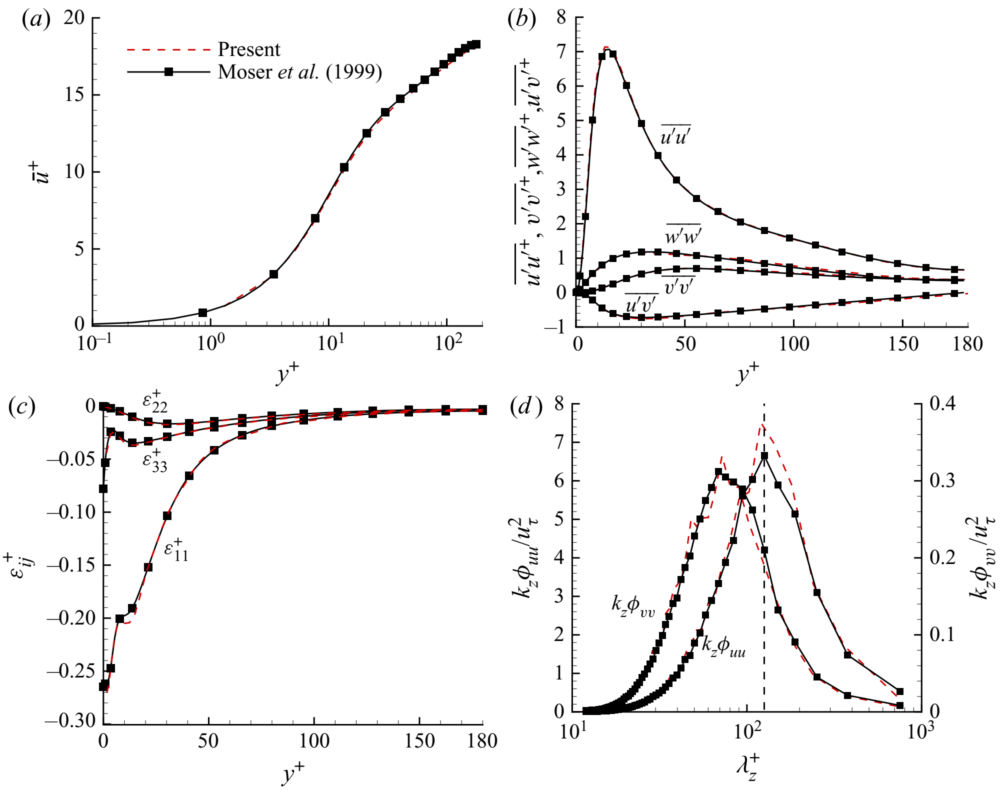

Figure 3. Comparison of turbulence statistics near the inlet with the DNS database of the fully developed channel flow at $Re_\tau = 180$ by Moser *et al.* (1999). Plots (*a–c*) are vertical profiles of the streamwise mean velocity (U), Reynolds stresses ($\overline{u'u'}$, $\overline{v'v'}$, $\overline{w'w'}$ and $\overline{u'v'}$) and dissipation rate ($\varepsilon_{ij} \equiv -2\nu\overline{\partial u_i'/\partial x_k \partial u_j'/\partial x_k}$), respectively. (*d*) Spanwise premultiplied energy spectra ($k_z\phi_{uu}$ and $k_z\phi_{vv}$) at $y^+ = 19$ (close to the peak location of $\overline{u'u'}$). The dashed vertical line marks the wavelength of $\lambda_z^+ = 126$.

(CFL) number was kept below 0.2. The simulation was first run for $330\delta/U_C$ to reach the statistical equilibrium state, which corresponds to 27.5 ‘flow-through’ times, i.e. $27.5L_i/U_C$. Subsequently, 1123 instantaneous flow fields sampled over a time period of $28L_i/U_C$ were stored for post-processing using MATLAB® scripts. The computations were performed in the CC Compute Cluster provided by the University of Manitoba. Approximately, 500 000 CPU hours were consumed for the present study.

In this paper, operator $\overline{(\cdot)}$ denotes averaging in both time and the homogeneous spanwise (z) direction whenever applicable, and the superscript $(\cdot)'$ represents the fluctuating component. As such, the instantaneous streamwise velocity can be decomposed as $u = \bar{u} + u'$. Additionally, angular brackets $\langle\cdot\rangle$ denote conditional averaging and subscript $(\cdot)_{rms}$ represents the root-mean-square value, e.g. $u'_{rms} = \overline{u'u'}^{1/2}$.

3. Results and discussion

3.1. *Instantaneous flow field and skin friction coefficients*

Figures 4(*a*) and 4(*b*) plot the isosurface of reverse flow ($u < 0$) in a typical instantaneous flow field near the FFS, which is also shown in a supplementary animation. In general, the reverse flows occur in irregular shaped volumes upstream and downstream of the leading

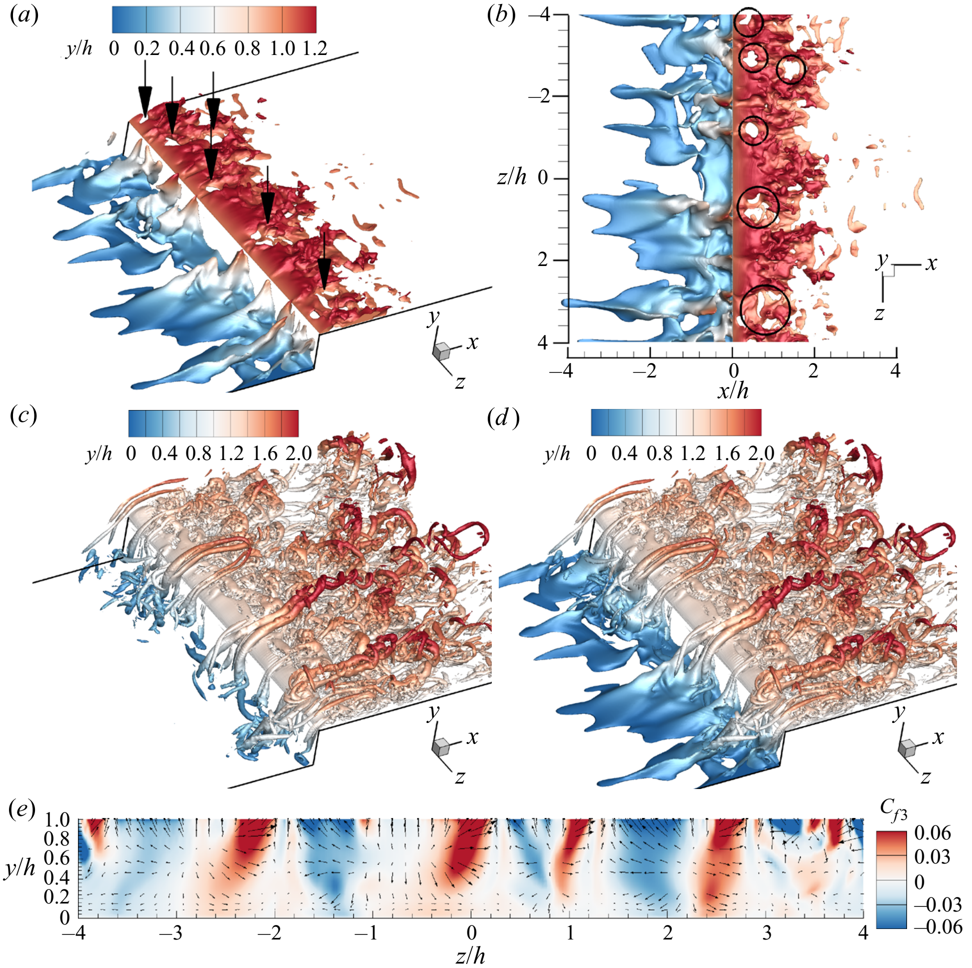

Figure 4. Characterization of a typical instantaneous flow field. (*a*) Isosurface of the reverse flow ($u < 0$) near the step. The thick arrows mark intermediate reattachment regions over the step. (*b*) Top view of (*a*). The black circles mark the same regions indicated using arrows in (*a*). (*c*) Isosurface of swirling strength $\lambda_{ci}h/U_C = 10$. (*d*) Superposition of the isosurfaces of the reverse flow and $\lambda_{ci}h/U_C = 10$. Note that (*a*,*b*) and (*c*,*d*) use different contour levels of y to highlight different features. (*e*) Contour of spanwise skin friction coefficient C_{f3} superimposed with the skin friction vectors (C_{f3}, C_{f2}). Not all vectors are plotted for clarity. An animation is also shown in a supplementary movie 1 available at https://doi.org/10.1017/jfm.2021.395.

edge of the step. The volume of reverse flow upstream of the step can extend across the entire height of the step. This is in line with the spillover of the separation bubble upstream of the FFS observed by Stüer *et al.* (1999), Wilhelm *et al.* (2003) and Pearson *et al.* (2013). The extremely high elevation of reverse flows upstream of the step occurs quasi-periodically in the spanwise direction. It is also interesting to note that over the FFS, reverse flow disappears in patches (marked using arrows and circles in figures 4(*a*) and 4(*b*), respectively). The x–y planes across these intermediate reattachment patches would exhibit dual separation bubbles over the step, which is reminiscent of the break-up event of the separation bubble over a forward-backward-facing step observed by Fang & Tachie (2019*b*). From the supplementary animation, the spillover of the separation bubble

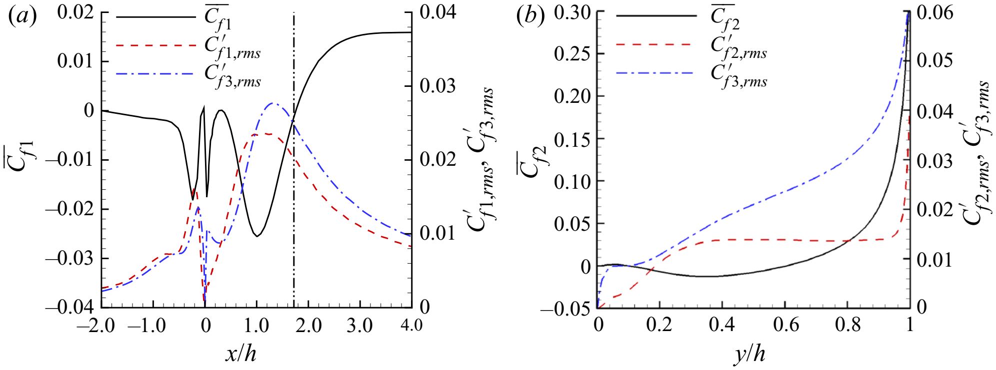

Figure 5. (*a*) Streamwise variation of $\overline{C_{f1}}$, $C'_{f1,rms}$ and $C'_{f3,rms}$ over the bottom wall and top surface of the step. The vertical dash-dot-dotted line marks the mean reattachment point. (*b*) Vertical variation of $\overline{C_{f2}}$, $C'_{f2,rms}$ and $C'_{f3,rms}$ on the frontal surface of the step.

upstream of the step tends to occur near the same spanwise location as the intermediate reattachment over the step.

Figures 4(*c*) and 4(*d*) show the vortical structures identified by the isosurface of λ_{ci}, which is defined as the imaginary part of the eigenvalues of the velocity gradient tensor (Zhou *et al.* 1999). From figure 4(*c*), the density of vortical structures suddenly increases as the step is approached, and the vortical structures leaning over the step are preferentially aligned in the streamwise-vertical planes. Downstream of the leading edge of the FFS, spanwise orientated vortical structures begin to appear, and eventually a 'forest' of hairpin-like structures appear. It is evident in figures 4(*d*) that the vortical structures leaning over the FFS coincide with the spillover of reverse flow upstream of the FFS.

Figure 4(*e*) plots the instantaneous skin friction coefficient over the frontal surface of the step. In the present paper, the instantaneous skin friction coefficient in the x_i direction is defined as $C_{fi} = \nu(\partial u_i/\partial n)|_{wall}/(U_C^2/2)$, where n denotes the wall normal direction. Note that in this paper, C_{fi} represents the instantaneous skin friction coefficient instead of the associated mean value as commonly used in the literature. It is evident in figure 4(*e*) that pairs of positive and negative C_{f3} occur, and the skin friction vectors (C_{f3}, C_{f2}) exhibit a pattern of alternating saddle and nodal points in the spanwise direction. This observation is similar to the oil-film visualization on the frontal surface of forward-backward-facing steps submerged in a turbulent channel flow by Martinuzzi & Tropea (1993). In accordance with figures 4(*b*) and 4(*e*), the spillover of reverse flow upstream of the step appears to be near the centre of each pair of positive and negative C_{f3} on the frontal surface of the step.

In view of the well-organized alternating positive and negative C_{f3} on the frontal surface of the step shown in figure 4(*e*), it is worthwhile further investigating the statistical properties of the skin friction coefficients near the step. While the mean $(\overline{C_{f1}})$ and root-mean-square $(C'_{f1,rms})$ values of streamwise skin friction induced by sharp-edged bluff bodies have been examined in the literature (e.g. Dianat & Castro 1984; Hattori & Nagano 2010), the corresponding spanwise skin friction has not been reported. Figure 5 presents the mean and root-mean-square values of all applicable skin friction coefficients on the bottom wall upstream of the step as well as the frontal and top surfaces of the step. From figure 5(*a*), $\overline{C_{f1}}$ has three local minima: one near the mean recirculation core in the upstream corner of the step, one immediately downstream of the leading edge and one near the core of the mean recirculation bubble over the step, which pattern is similar to

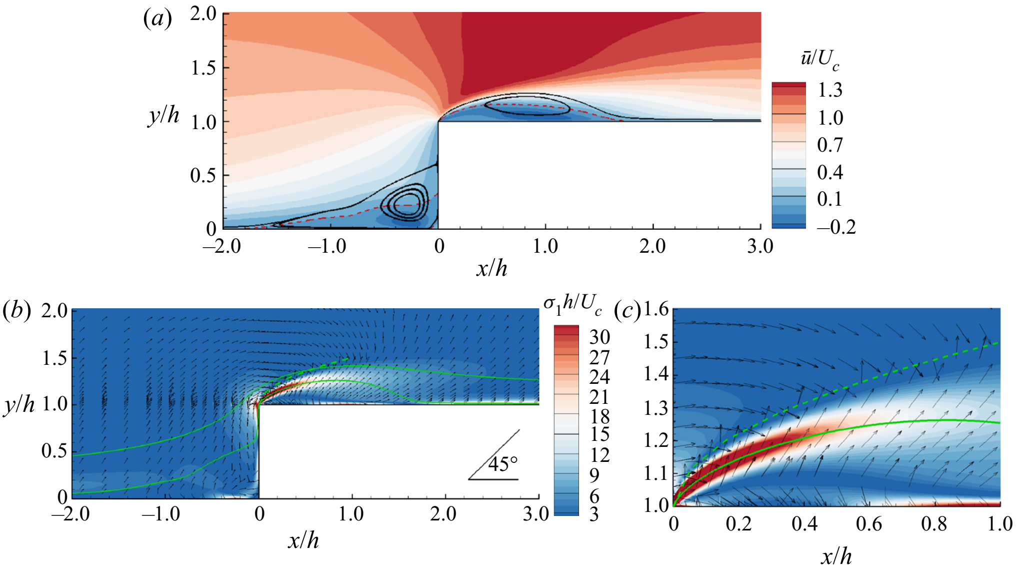

Figure 6. (a) Contour of streamwise mean velocity ($\bar{u}$) superimposed with representative mean streamlines (solid lines). The dashed isopleth is at $\bar{u} = 0$. (b) Magnitudes (contour) and directions (vectors) of principal stretching superimposed with representative mean streamlines (solid lines). The dashed line is a function of $y/h = 0.5\sqrt{x/h} + 1.0$, and is denoted by PSL for conciseness in the present paper. Plot (c) magnifies the region in (b) near the leading edge of the step.

that observed by Hattori & Nagano (2010). The magnitudes of $C'_{f1,rms}$ and $C'_{f3,rms}$ are close to each other upstream of the step ($x/h < 0$), while the latter becomes slightly larger than the former for $x/h > 1.0$. The comparable peak values of $C'_{f1,rms}$ and $C'_{f3,rms}$ suggest that the spanwise fluctuating flow motion can be as dynamically significant as the streamwise counterpart. Furthermore, as seen in figure 5(b), $C'_{f3,rms}$ is significantly larger than $C'_{f2,rms}$ on the frontal surface of the step. In fact, $C'_{f3,rms}$ monotonically increases in the vertical direction and the peak value (at the leading edge of the step) is more than twice the maximum value of $C'_{f1,rms}$. The high levels of $C'_{f3,rms}$ on the frontal surface of the step indicate that the alternating positive and negative C_{f3} observed in figure 4(e) represents a strong and coherent flow structure at play.

3.2. *Turbulence statistics*

Figure 6(a) shows the contour of streamwise mean velocity ($\bar{u}$) and mean streamlines near the FFS. Two distinct mean separation bubbles occur upstream of and over the step. Upstream of the step, the mean separating point on the bottom wall is at $x/h = -2.0$, while the stagnation point on the frontal surface is at $y/h = 0.6$. These locations agree well with the separating point ($x/h \in [-1.73, -1.93]$) and stagnation point ($y/h \in [0.59, 0.61]$) observed by the DNS study of Hattori & Nagano (2010) for an FFS submerged in an oncoming TBL, but are different than those reported in experimental and large-eddy simulation studies of FFS flows (Moss & Baker 1980; Addad *et al.* 2003; Graziani *et al.* 2018; Fang & Tachie 2020). For instance, Fang & Tachie (2020) and Graziani *et al.* (2018) observed that the mean separation on the bottom wall occurs at $x/h = -0.85$ and $x/h = -1.0$, respectively, while the mean stagnation point on the frontal surface is at $y/h = 0.45$ and $y/h = 0.55$, respectively. It is also observed in figure 6(a) that the mean reattachment length over the step is $1.72h$. This value is comparable to 1.82–$1.86h$ and $1.6h$ reported by Hattori & Nagano (2010) and Fang & Tachie (2020), respectively, but significantly smaller than that ($3.2h$) observed by Graziani *et al.* (2018).

Following Fang & Tachie (2020), the mean flow field is further investigated in terms of the topological characteristics of the mean shear, i.e. $S_{ij} = (\partial \bar{u}_i/\partial x_j + \partial \bar{u}_j/\partial x_i)/2$. In the present study, all non-zero components of S_{ij}, which are S_{11}, S_{12} and S_{22}, are in the x–y plane due to spanwise homogeneity, and are hereafter denoted by $\boldsymbol{S_{xy}}$ for conciseness. The eigendecomposition of $\boldsymbol{S_{xy}}$ is expressed as

$$\boldsymbol{S_{xy}} = \begin{bmatrix} \dfrac{\partial \bar{u}}{\partial x} & \dfrac{1}{2}\left(\dfrac{\partial \bar{u}}{\partial y} + \dfrac{\partial \bar{v}}{\partial x}\right) \\ \dfrac{1}{2}\left(\dfrac{\partial \bar{u}}{\partial y} + \dfrac{\partial \bar{v}}{\partial x}\right) & \dfrac{\partial \bar{v}}{\partial y} \end{bmatrix} = \boldsymbol{Q}\begin{bmatrix} \sigma_1 & 0 \\ 0 & \sigma_2 \end{bmatrix}\boldsymbol{Q}^{\mathrm{T}}. \tag{3.1}$$

Here, superscript $(\cdot)^{\mathrm{T}}$ denotes the transpose of a matrix, σ_1 and σ_2 are two eigenvalues of $\boldsymbol{S_{xy}}$, and the corresponding eigenvectors are indicated by the first and second column of $\boldsymbol{Q}$, respectively. Since $\boldsymbol{S_{xy}}$ is a symmetric real matrix, its eigenvalues are real and eigenvectors are orthogonal. Due to incompressibility (equation (2.1)), $\sigma_1 + \sigma_2 = \mathrm{trace}(\boldsymbol{S_{xy}}) = \partial \bar{u}/\partial x + \partial \bar{v}/\partial y = 0$ holds. Without loss of generality, we define σ_1 as the positive eigenvalue of $\boldsymbol{S_{xy}}$, indicating the strength of principal stretching. Consequently, the first column of $\boldsymbol{Q}$ defines the direction of principal stretching, and is restricted to be between -90° and 90°, since $-\boldsymbol{Q}$ also defines the eigenvectors.

Figures 6(*b*) and 6(*c*) characterize the magnitudes and directions of principal stretching in the vicinity of the step. The present topology of principal stretching is similar to that observed by Fang & Tachie (2020), in spite of significantly different upstream flow conditions. In the region sufficiently upstream of the leading edge (say $x/h < -1.0$ or $x/h > 2.0$), the principal stretching is generally at 45° with the streamwise direction, resembling that in a canonical TBL or fully developed channel flow. As the step is approached below the step height ($y/h < 1$), principal stretching becomes steeper and eventually is aligned vertically near the frontal surface. Along the mean streamline deflected over the step, the principal stretching is approximately parallel with the mean streamline in the region slightly upstream of the leading edge of the step before becoming horizontally aligned directly above the leading edge. As evident in figure 6(*c*), the principal stretching switches orientation abruptly at a location given by a curved line emanating from the leading edge. This curved line fits well into the function of $y/h = 0.5\sqrt{x/h} + 1.0$. In Fang & Tachie (2020) the principal stretching switches orientation abruptly near a straight line at 29° with the streamwise direction. For conciseness, the dashed curve in figure 6(*c*) is hereafter denoted by PSL (as in 'principal stretching line').

Figure 7 presents the contours of all non-trivial second-order moment statistics of the fluctuating velocities and vorticities near the step. Note that, following Fang & Tachie (2019*b*) and Fang & Tachie (2020), the presented statistics in the x–y plane are defined in the curvilinear coordinate system along the mean streamlines so as to reflect the mean streamline curvature. (Many useful counterpart flow statistics defined in the conventional Cartesian coordinate system extracted from the present DNS database have been provided in Fang, Tachie & Bergstrom (2021).) Specifically, the second-order moment statistics of fluctuating vorticities tangential and perpendicular to the mean streamline can be

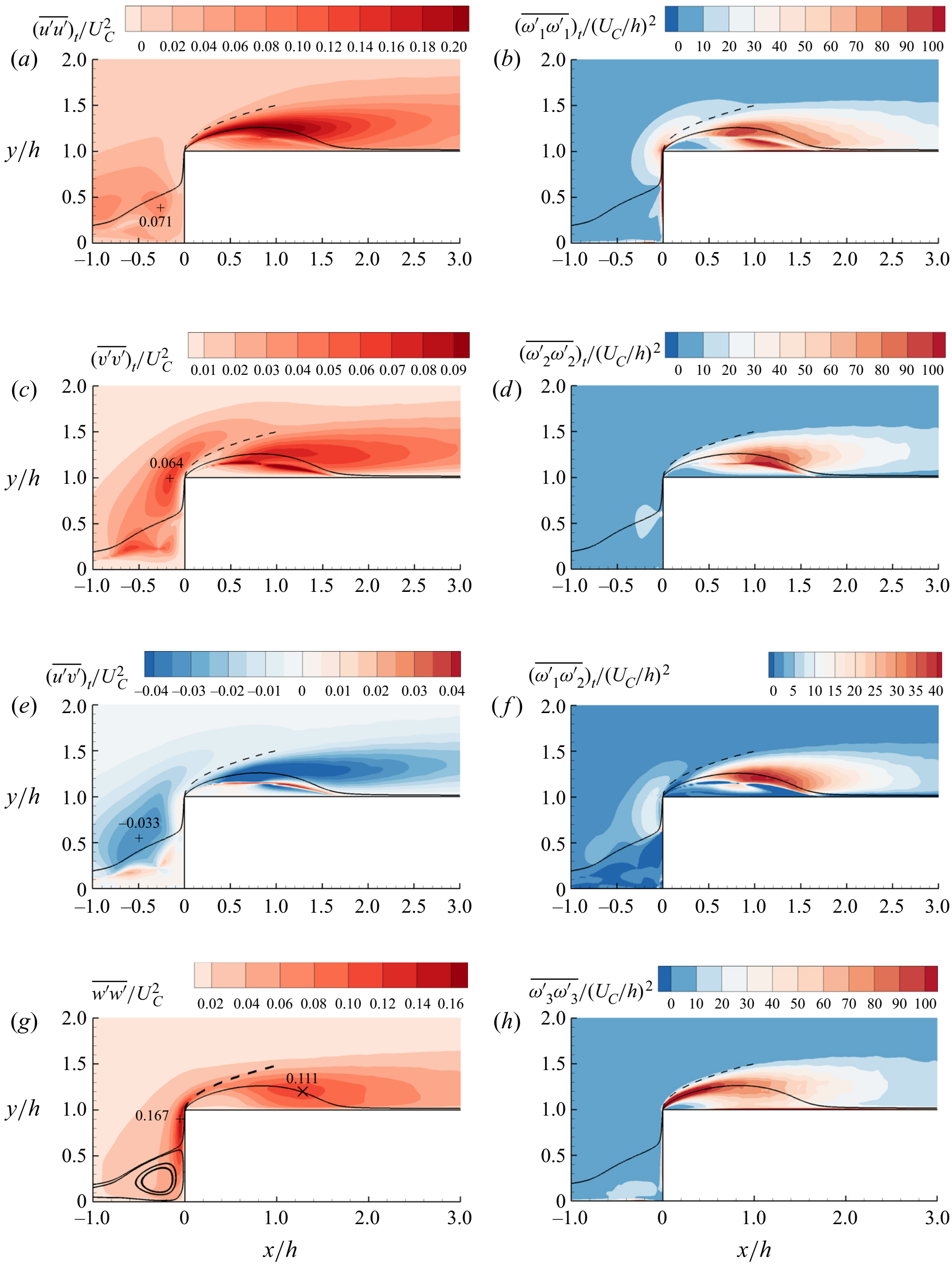

Figure 7. Contours of mean-square values of fluctuating velocity and vorticity along and perpendicular to the mean streamlines superimposed with mean separating streamlines (solid lines): (*a*) $(\overline{u'u'})_t$, (*b*) $(\overline{\omega'_1\omega'_1})_t$, (*c*) $(\overline{v'v'})_t$, (*d*) $(\overline{\omega'_2\omega'_2})_t$, (*e*) $(\overline{u'v'})_t$, (*f*) $(\overline{\omega'_1\omega'_2})_t$, (*g*) $\overline{w'w'}$ and (h) $\overline{\omega'_3\omega'_3}$. In (*a*,*c*,*e*,*g*), symbol + marks the local peak upstream of the step. The dashed line represents the location of the PSL.

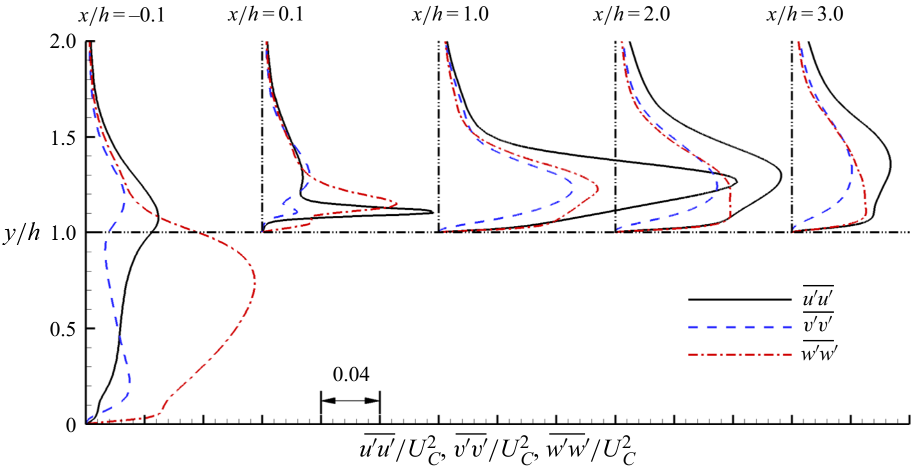

Figure 8. Vertical profiles of Reynolds stresses $\overline{u'u'}$, $\overline{v'v'}$ and $\overline{w'w'}$ at $x/h = -0.1$, 0.1, 1.0, 2.0 and 3.0.

calculated as follows:

$$(\overline{\omega_1'\omega_1'})_t = \overline{\omega_1'\omega_1'}\cos^2(\theta) + \overline{\omega_2'\omega_2'}\sin^2(\theta) + \overline{\omega_1'\omega_2'}\sin(2\theta), \tag{3.2a}$$

$$(\overline{\omega_2'\omega_2'})_t = \overline{\omega_2'\omega_2'}\cos^2(\theta) + \overline{\omega_1'\omega_1'}\sin^2(\theta) - \overline{\omega_1'\omega_2'}\sin(2\theta), \tag{3.2b}$$

$$(\overline{\omega_1'\omega_2'})_t = \overline{\omega_1'\omega_2'}\cos(2\theta) - \left(\overline{\omega_1'\omega_1'} - \overline{\omega_2'\omega_2'}\right)\sin(2\theta)/2. \tag{3.2c}$$

In the above equation, subscript $(\cdot)_t$ denotes a variable in the curvilinear coordinate system along the mean streamlines, and θ is the angle between mean velocity and the streamwise direction. The corresponding Reynolds stresses defined in the curvilinear coordinate system along the mean streamline ($(\overline{u'u'})_t$, $(\overline{v'v'})_t$ and $(\overline{u'v'})_t$) can be obtained by substituting ω_1' and ω_2' with u' and v', respectively, in the above equations.

As seen in figures 7(*a*)–7(*f*), these statistics show abrupt variations in a narrow area connecting the leading edge and the mean reattachment point within the mean separation bubble. This narrow area is in close vicinity of the isopleth of $\bar{u} = 0$, and the associated abrupt variations of statistics are a manifestation of the abrupt variation in the orientation of the mean streamlines. Moreover, the elevated levels of the plotted statistics over the step are confined downstream of the PSL. There exists an area of elevated levels of $(\overline{v'v'})_t$ slightly upstream of the leading edge of the step. The peak value of $(\overline{v'v'})_t$ upstream of the step is much larger than that of $(\overline{u'u'})_t$ at the same location. It is therefore concluded that, in the region immediately upstream of the step, the fluctuating velocity perpendicular to the mean streamline dominates over that parallel with the mean streamline. This observation has also been made in our recent experimental study of turbulent separation induced by an FFS (Fang & Tachie 2020). In Fang & Tachie (2020), based on the planar PIV measurement, it was speculated that the dominance of $(\overline{v'v'})_t$ upstream of the leading edge is accompanied with the dominance of fluctuating vorticity along the mean streamline. This speculation is now confirmed. Indeed, by comparing figures 7(*b*), 7(*d*) and 7(*h*), the dominance of fluctuating vorticity parallel to the mean streamline $(\overline{\omega_1'\omega_1'})_t$ immediately upstream of the step is apparent. It is also important to notice in figure 7 that the significant values of $(\overline{\omega_1'\omega_1'})_t$ immediately upstream of the step is also accompanied by elevated levels of $\overline{w'w'}$ in that vicinity. The upstream peak of $\overline{w'w'}$ is 50 % larger than the corresponding downstream peak, and is evidently larger than the upstream peak values of $(\overline{u'u'})_t$ and $(\overline{v'v'})_t$. It is emphasized that, to our best knowledge, the significance of the spanwise Reynolds normal stress $\overline{w'w'}$ near an FFS has not been reported before.

Figure 8 examines the streamwise variation of the vertical profiles of all three Reynolds normal stresses ($\overline{u'u'}$, $\overline{v'v'}$ and $\overline{w'w'}$). From the figure, the peak value of $\overline{w'w'}$ is larger than those of the other two Reynolds normal stresses in the region slightly upstream of the leading edge ($x/h = -0.1$), and becomes lower than the peak values of $\overline{u'u'}$ over the step. In the near-wall region (say $y/h < 1.1$) over the step, $\overline{w'w'}$ dominates over $\overline{u'u'}$ and $\overline{v'v'}$ near the leading edge ($x/h = -0.1$), and becomes closes to $\overline{u'u'}$ for $x/h \geq 1.0$. On the other hand, $\overline{w'w'}$ is fairly close to $\overline{v'v'}$ in the region further away from the top surface of the step (say $y/h > 1.4$). It is also noted in figure 8 that $\overline{v'v'}$ possesses two local peaks in the vertical direction at $x/h = -0.1$ and 0.1, and shows single peaks that coincide with the peak locations of $\overline{u'u'}$ in the region of $x/h \geq 1.0$. It is a common practice in experimental studies to estimate the out-of-plane Reynolds normal stress by averaging the two in-plane Reynolds normal stresses (i.e. $\overline{w'w'} \approx (\overline{u'u'} + \overline{v'v'})/2$), when only streamwise and vertical components of the velocity field are available. For example, Kim, Ji & Seong (2003) and Schröder *et al.* (2020) used this estimation to further approximate the turbulent kinetic energy as $(\overline{u_i'u_i'})/2 \approx 3(\overline{u'u'} + \overline{v'v'})/4$ for the turbulent flow separations induced by surface-mounted bluff bodies. It is evident from figure 8 that these estimations are not valid for the flow separation induced by an FFS.

3.3. *Two-point correlation*

In the previous section the significance of $(\overline{v'v'})_t$ and $(\overline{w'w'})$ upstream of the leading edge of the step is demonstrated in figure 7. Based on the linear instability analysis performed by Lanzerstorfer & Kuhlmann (2012), without incoming turbulence, the most unstable mode over an FFS possesses the maximum energy along the mean separating streamline. Indeed, for flow separation subjected to incoming laminar flows, the turbulence intensity is commonly observed to be concentrated along the separated shear layer and peaks in the rear part of the separation bubble (Kiya & Sasaki 1983; Djilali & Gartshore 1991; Alam & Sandham 2000; Yang & Voke 2001). This is clearly not the case in figure 7. It is deduced that the elevated $(\overline{v'v'})_t$ and $(\overline{w'w'})$ upstream of the step signify the interaction between incoming turbulence motion and the step. While Fang & Tachie (2020) has examined the turbulence structure associated with the peak of $(\overline{v'v'})_t$, it was limited to 2-D information derived from planar PIV measurements. The peak value of $(\overline{w'w'})$ near the frontal surface of FFS has not been recognized in the literature, and the associated turbulence structure is unknown. In this section we examine the 3-D turbulence structure associated with the peak $(\overline{v'v'})_t$ and $(\overline{w'w'})$ upstream of the leading edge of the step using two-point correlation, which is expressed as

$$R_{\vartheta\zeta} = \frac{\overline{\vartheta'(\boldsymbol{X}_{ref})\zeta'(\boldsymbol{X}_{ref} + \boldsymbol{\Delta X})}}{\vartheta'_{rms}(\boldsymbol{X}_{ref})\zeta'_{rms}(\boldsymbol{X}_{ref} + \boldsymbol{\Delta X})}. \tag{3.3}$$

Here, ϑ and ζ represent two arbitrary variables such as v_t and w, while $\boldsymbol{X}_{ref}$ and $\boldsymbol{\Delta X}$ are the reference position and relative displacement, respectively.

Figures 9 plots the contours of two-point autocorrelations $R_{vv,t}$ ($\vartheta = \zeta = v_t$ in (3.3)) and R_{ww} ($\vartheta = \zeta = w$ in (3.3)) with the reference point at $(x/h, y/h) = (-0.16, 0.97)$, where $(\overline{v'v'})_t$ peaks. As seen in figures 9(*a*) and 9(*b*), the isopleths of $R_{vv,t}$ and R_{ww} tend to

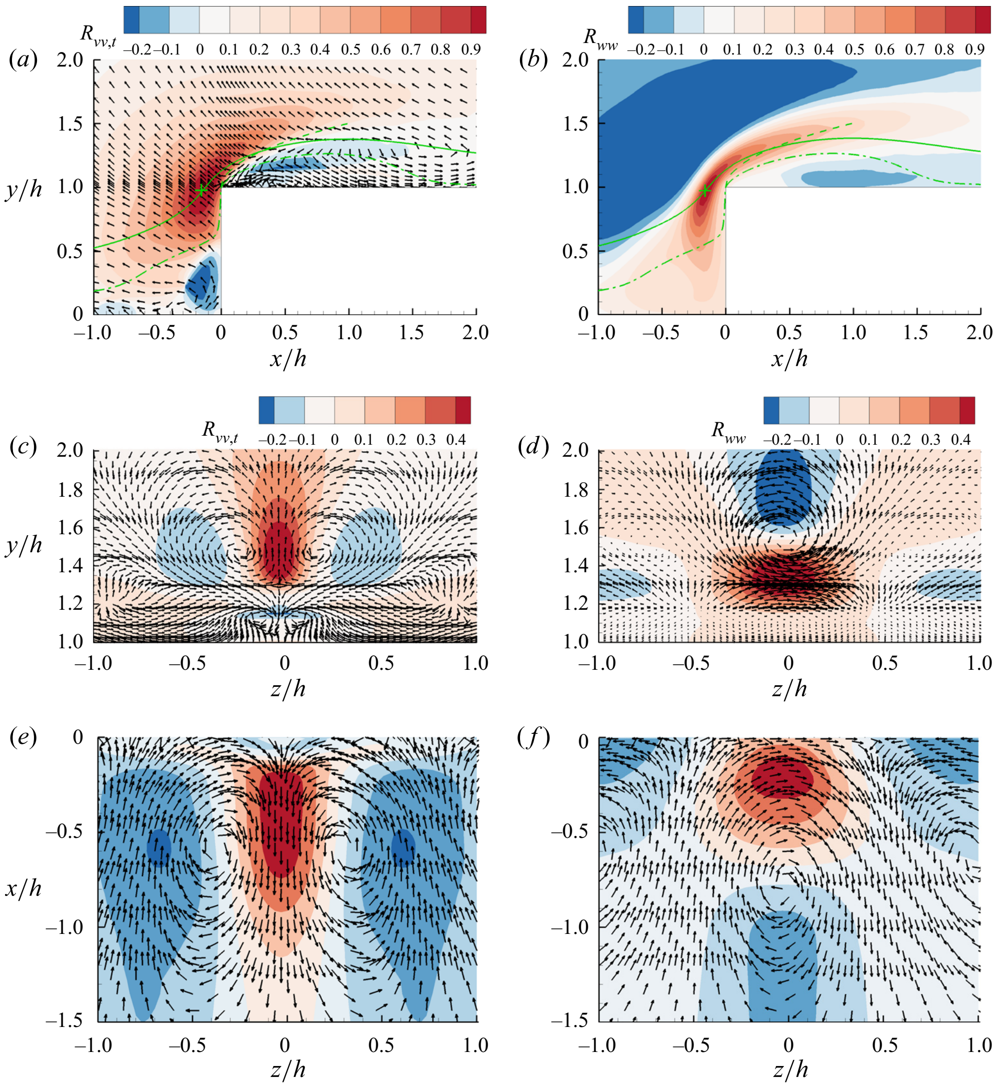

Figure 9. Contours of the two-point autocorrelations (*a*,*c*,*e*) $R_{vv,t}$ and (*b*,*d*,*f*) R_{ww} superimposed with in-plane LSE vectors with the reference point at $(x/h, y/h, z/h) = (-0.16, 0.97, 0.00)$ (marked using +): (*a*,*b*) the x–y plane crossing the reference point, (*c*,*d*) the z–y plane at $x/h = 0.3$ and (*e*,*f*) the z–x plane at $y/h = 0.5$. In (*a*,*b*), the dashed, dash-dotted and solid lines represent the location of the PSL, the mean separating streamline and the mean streamline passing the reference point, respectively. The vectors are absent in (*b*) because the two-point correlations R_{wu} and R_{wv} are zero in the plane due to spanwise homogeneity. The legends in (*e*,*f*) are the same as those in (*c*,*d*), respectively. All vectors are normalized to be of unit length, and not all vectors are shown for clarity. Note that only 25 % of the entire spanwise domain is shown here.

extend along the mean streamline traced from the reference point, while their magnitudes are abruptly reduced downstream of the PSL. Additionally, the significant positive values of $R_{vv,t}$ extend more in the upstream direction than R_{ww}. From figure 9(*c*–*f*), the positive valued $R_{vv,t}$ and R_{ww} in the reference plane are flanked by negative valued counterparts in the spanwise neighbourhood.

Figure 9 also plots the in-plane linear stochastic estimation (LSE) (Adrian & Moin 1988) vectors conditioned on v'_t and w' at the same reference point as the contours of autocorrelations. These LSE vectors are equivalent to the vectors of two-point correlations, and represent the turbulence structure associated with the condition event (Fang & Tachie 2019*a*; Kevin & Hutchins 2019). For instance, the vectors in figure 9(*a*) are $(R_{vt,u}, R_{vt,v})$. Here, $R_{vt,u}$ is calculated by letting $\vartheta = v_t$ and $\zeta = u$ in (3.3), and so on for $R_{vt,v}$. As seen in figure 9(*a*), the LSE vectors point backwards at approximately 45° upstream of the step, and change directions abruptly near the PSL. The LSE vectors also exhibit a spanwise vortex above the mean reattachment point. As seen in figure 9(*c*), in the cross-stream (z–y) plane, the LSE vectors exhibit two pairs of opposite-signed counter-rotating vortices around $y/h = 1.5$ and $y/h = 1.2$, respectively. Although not shown here, the top pair of counter-rotating vortices in figure 9(*c*) is connected to a pair of vertically orientated vortices upstream of the step shown in figure 9(*e*). In other words, the LSE vectors form a pair of counter-rotating vortices leaning over the step. This is consistent with the conclusion from figure 7 that the peak $(\overline{v'v'})_t$ upstream of the leading edge is associated with fluctuating vorticity parallel to the mean streamline. It is also worth mentioning that Fang *et al.* (2021) performed proper orthogonal decomposition (POD) analysis using the present DNS database, and showed the first POD mode similar to the LSE vectors in figure 9(*a*). Fang *et al.* (2021) also used LSE to show the first POD mode is associated with a 3-D turbulence structure similar to that demonstrated in figures 9(*c*) and 9(*e*). Furthermore, it is interesting to see in figures 9(*d*) and 9(*f*) that the LSE vectors conditioned on w' show structures similar to one side of those in figures 9(*c*) and 9(*e*). For instance, in figure 9(*d*) two opposite-signed streamwise vortices occur around $y/h = 1.6$ and $y/h = 1.2$, respectively, in the cross-stream plane over the step.

3.4. *Unsteadiness of the turbulent separation bubbles*

In the literature a low-frequency flapping motion has been observed in turbulent separation bubbles induced by geometry (Eaton & Johnston 1982; Pearson *et al.* 2013; Thacker *et al.* 2013; Graziani *et al.* 2018; Fang & Tachie 2019*b*,*a*), adverse pressure gradients (Mohammed-Taifour & Weiss 2016) and shock waves (Humble, Scarano & Van Oudheusden 2009). It is worth noting here that for convenience and conciseness in the subsequent discussion, we use ‘flapping motion’ to refer to a sequence of enlargement and contraction of separation bubble regardless of the contexts, although the term ‘breathing motion’ is perhaps more appropriate for separations with unsteady separating points (e.g. Mohammed-Taifour & Weiss (2016). There is no consensus on the underlying mechanism of the flapping motion. For instance, Pearson *et al.* (2013), Fang & Tachie (2019*b*), Fang & Tachie (2019*a*) and Fang & Tachie (2020) attributed the flapping motion of separation bubbles induced by surface-mounted bluff bodies to the incoming streamwise-elongated streaky structures, while Eaton & Johnston (1982) attributed the unsteadiness of the separation bubble behind a backward-facing step to the instantaneous imbalance between the entrainment of the shear layer and reinjection near the reattachment point. It should also be noted here that all the aforementioned investigations were based on either planar PIV or hot-wire measurements.

Following Pearson *et al.* (2013), Fang & Tachie (2019*b*), Fang & Tachie (2019*a*) and Fang & Tachie (2020), the instantaneous reverse flow areas upstream and downstream of the FFS are used to track the instantaneous sizes of separation bubbles upstream of and over the step, which are, respectively, defined as

$$A_F(z,t) = \int_0^h \int_{-24h}^0 \mathscr{H}(u(x,y,z,t))\,\mathrm{d}x\,\mathrm{d}y \tag{3.4}$$

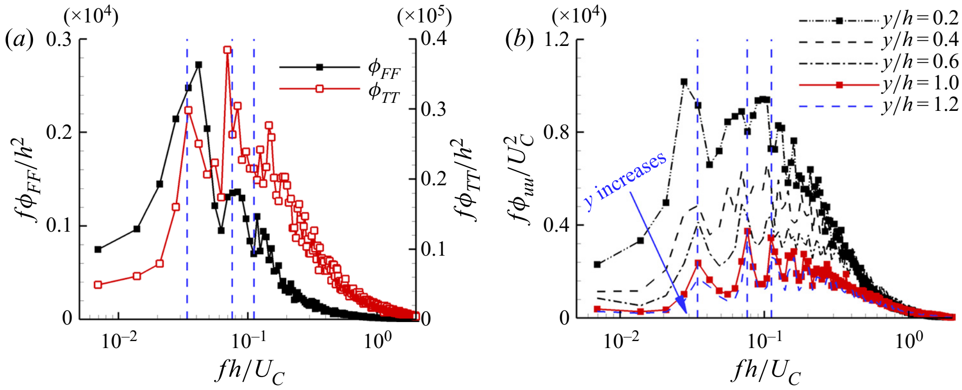

Figure 10. (*a*) Premultiplied frequency spectra of A_F (ϕ_{FF}) and A_T (ϕ_{TT}). (*b*) Premultiplied frequency spectra of the streamwise velocities at different elevations in the inlet plane. The three vertical dashed lines mark the frequencies $fh/U_C = 0.034$, 0.076 and 0.112 from the left to right. The resolved frequencies are marked using symbols for selected lines to facilitate visualization.

and

$$A_T(z, t) = \int_h^{2h} \int_0^{36h} \mathscr{H}(u(x, y, z, t))\, \mathrm{d}x\, \mathrm{d}y. \tag{3.5}$$

In the above equations, an auxiliary function $\mathscr{H}$ is defined as $\mathscr{H}(\xi) = 0$ if $\xi \geq 0$ and $\mathscr{H}(\xi) = 1$ if $\xi < 0$. In this paper the reverse flow areas upstream (A_F) and downstream (A_T) of the FFS are defined as functions of both the spanwise location (z) and time (t), so as to reflect the 3-D spatio-temporal unsteadiness of separation bubbles observed in the supplementary movie for figure 4. We note that in the previous experimental studies using planar PIV systems, the simultaneous access to both the spanwise (z) and temporal (t) variations of the separation bubble was impossible. The available information of flapping motion of reverse flows from previous planar PIV experiments can be interpreted as a spanwise-averaged counterpart of (3.4) and (3.5), assuming a spanwise homogeneity. The 3-D spatio-temporal unsteadiness of the turbulent separation bubbles are analysed in the following two subsections.

3.4.1. *Temporal characteristics of the turbulent separation bubbles*

It is evident from the supplementary animation of figure 4 that the volumes of reverse flow vary in time. To further quantitatively investigate the temporal variation of the separation bubbles, the frequency spectra of A_F and A_T are calculated and shown in figure 10(*a*). To calculate these frequency spectra, the temporal signals at 60 evenly distributed spanwise locations were collected over a time period of $144h/U_C$. Fourier transformation was performed for each temporal signal, and the spectra were obtained by averaging over these 60 samples in the spanwise direction. As such, the resolved frequencies are multiples of $0.0069U_C/h$ (which are also visualized by showing symbols in the figure), and this eventually defines the accuracy of any identifiable frequencies. As shown in figure 10(*a*), the values of $f\phi_{FF}$ and $f\phi_{TT}$ near the lowest resolved frequency are much lower than the corresponding peak values. This indicates that any frequency lower than $0.0069U_C/h$ is of negligible importance, and the presented frequency spectra well capture the temporal variation of the two separation bubbles.

It is evident in figure 10(a) that both separation bubbles possess local peak frequencies around $fh/U_C = 0.033$ and 0.076. Although not shown here, it is worth mentioning that the local peak frequency around $fh/U_C = 0.076$ persists even if the window size of Fourier transformation is halved, which gives twice as many samples of spectra for averaging. These frequencies ($fh/U_C = 0.033$ and 0.076) do not reflect the well-known low-frequency flapping motion and high-frequency vortex shedding motion residing in the separation bubble without the perturbation of incoming turbulence. Indeed, for the separation bubbles induced by bluff bodies subjected to incoming uniform flows, the separation bubble features a periodic sequence of enlargement and contraction of the separation bubble at a low-frequency range $fL_r/U_C \in [0.08, 0.2]$ and periodic vortex shedding motion around $fL_r/U_C \in [0.5, 1.0]$ (where L_r is the mean reattachment length) (Kiya & Sasaki 1983; Tafti & Vanka 1991; Hudy, Naguib & Humphreys 2003). These frequency ranges are much larger than the frequencies residing in the present two separation bubbles. Specifically, $fh/U_C = 0.034$ and 0.076 correspond to $fL_r/U_C = 0.020$ and 0.044, respectively, for the separation bubble over the step, and they correspond to $fL_r/U_C = 0.017$ and 0.038 for the separation bubble upstream of the step.

Figure 10(b) plots the frequency spectra of the streamwise fluctuating velocity for the incoming flow. To prevent the possibility of the unphysical oscillating frequency spectra due to lack of samples, the DNS of turbulent channel flow was ran separately for a long time, and the convergence of the frequency spectra in figure 10(b) is confirmed by using the temporal signal at 60 homogeneous locations over a time period of $1280h/U_C$. As shown in figure 10(b), the local peak frequency at $fh/U_C = 0.034$ persists for $y/h \geq 0.4$, and multiple harmonics of the frequency $fh/U_C = 0.033$ are manifest for $y/h \geq 0.6$. For instance, the frequency spectrum at the step height ($y/h = 1.0$) exhibits local peak frequencies at $fh/U_C = 0.034, 0.076, 0.112, 0.155, 0.194$ and so on. For the fully developed turbulent channel flow at $Re_\tau = 590$, by performing POD in the frequency–wavenumber space, Muralidhar *et al.* (2019) observed the dominant frequency at $f^+ = 0.0044$ and also noted the occurrence of harmonics. Our results in figure 10 show that the dominant frequency ($fh/U_C = 0.034$ which corresponds to $f^+ = 0.0063$) for the turbulent channel flow at $Re_\tau = 180$ is relatively higher than that at $Re_\tau = 590$.

By comparing figures 10(a) and 10(b), it becomes clear that the dominant frequencies ($fh/U_C = 0.034$ and 0.076) of the separation bubbles mirror the dominant and harmonic frequencies of the streamwise velocity in the incoming flow. In fact, $f\phi_{FF}$ and $f\phi_{TT}$ also exhibit a localized peak around $fh/U_C = 0.112$, which also manifests in the incoming flow as a harmonic. Additionally, as seen in figure 10(a), the frequency $fh/U_C = 0.034$ is more dominant than the frequency $fh/U_C = 0.076$ for the upstream separation bubble, and this order of dominance flips for the separation over the step. The dominance between $fh/U_C = 0.034$ and 0.076 also flips as y increases in the frequency spectra of u' in the incoming flow as shown in figure 10(b).

To further investigate the interaction between the upstream and downstream separation bubbles, figure 11(a) shows the temporal cross-correlation of A'_F and A'_T, which is defined as

$$R_{FT}(\Delta t) = \frac{\overline{A'_F(t)A'_T(t+\Delta t)}}{A'_{F,rms}A'_{T,rms}}. \tag{3.6}$$

From the figure, R_{FT} in the present study and Graziani *et al.* (2018) exhibit a similar pattern, where a single negative peak is dominant, in spite of a noticeable quantitative difference. Specifically, the peak magnitude of R_{FT} in the present study is approximately -0.28 and with a time delay of $\Delta t = 2.9h/U_C$, while that in Graziani *et al.* (2018)

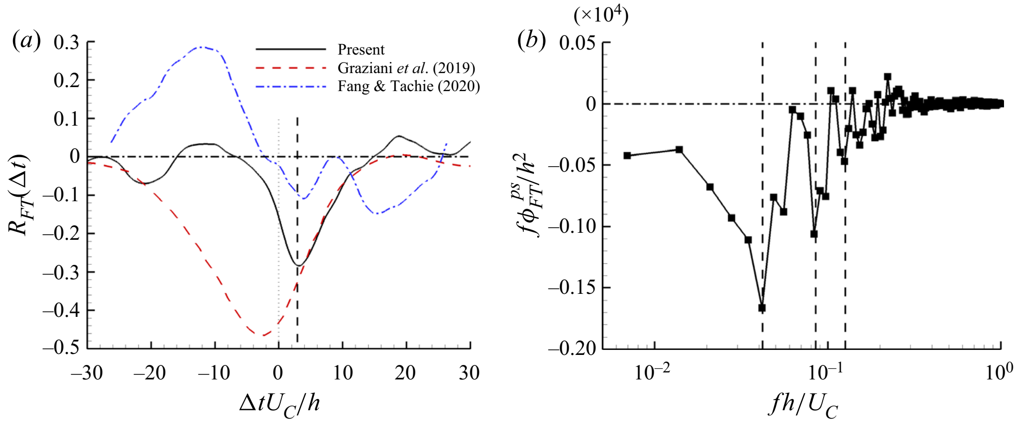

Figure 11. (*a*) Temporal cross-correlation ($R_{FT}(\Delta t)$) of A'_F and A'_T. The dashed vertical line marks the time difference $\Delta t U_C/h = 2.9$. Note that U_C is replaced by free-stream velocity in presenting the data from Graziani *et al.* (2018) and Fang & Tachie (2020). (*b*) Premultiplied phase-shifted co-spectrum $\phi^{ps}_{FT}(f, \Delta t = 2.9h/U_c)$. The three vertical dashed lines mark the frequencies fh/U_C = 0.042, 0.082 and 0.126 from left to right. The resolved frequencies are marked using solid symbols.

is approximately −0.46 and occurs at $\Delta t = -2.0h/U_C$. The negatively valued R_{FT} in the present study and Graziani *et al.* (2018) suggest that the upstream and downstream separation bubbles tend to be opposite in phase, i.e. an expansion of the upstream separation bubble is proceeded by a contraction of the downstream separation bubble. It is further noted in figure 11(*a*) that R_{FT} in Fang & Tachie (2020) is qualitatively and quantitatively different from those in the present study and Graziani *et al.* (2018). For example, R_{FT} can be of a positive peak around $\Delta t = -12.0h/U_C$. This indicates the significant events where both the upstream and downstream separation bubbles are expanded/contracted with a noticeable time delay.

Following Fang & Tachie (2019*b*), the contribution of different frequencies to $R_{FT}(\Delta t)$ is quantified using a phase-shifted co-spectrum, which is defined as

$$\phi^{ps}_{FT}(f, \Delta t) = \overline{\widehat{A_F}(f)\left[\widehat{A_T}(f)\exp(2\pi \mathrm{i} f \Delta t)\right]^*} + \overline{\widehat{A_F}^*(f)\widehat{A_T}(f)\exp(2\pi \mathrm{i} f \Delta t)}. \tag{3.7}$$

In the above equation, $\mathrm{i} \equiv \sqrt{-1}$, while the operators $\widehat{(\cdot)}$ and $(\cdot)^*$ represent the Fourier coefficient and complex conjugate, respectively, so that $R_{FT}(\Delta t) = \int \phi^{ps}_{FT}(f, \Delta t)\, \mathrm{d}f$. Figure 11(*b*) plots $f\phi^{ps}_{FT}$ with $\Delta t = 2.9h/U_C$ to further investigate the interaction between the two separation bubbles amongst different frequencies. From the figure, $f\phi^{ps}_{FT}$ possesses a dominant frequency at $fh/U_C = 0.042$, and also exhibits significant peaks at harmonic frequencies ($fh/U_C = 0.082$ and 0.126). By comparing figures 10 and 11, the two separation bubbles interact with each other at the dominant and harmonic frequencies similar to those from the incoming flow.

3.4.2. *Spatial characteristics of the turbulent separation bubbles*

As demonstrated in figure 4 along with the supplemented animation, reverse flow occurs in irregular shaped volumes that vary significantly in time and spanwise direction. To investigate the spatial variations of reverse flow, figure 12 shows the probability density functions (p.d.f.s) of the spatial extents and areas of the reverse flows upstream and downstream of the step in the x–y plane. Note that these p.d.f.s were calculated

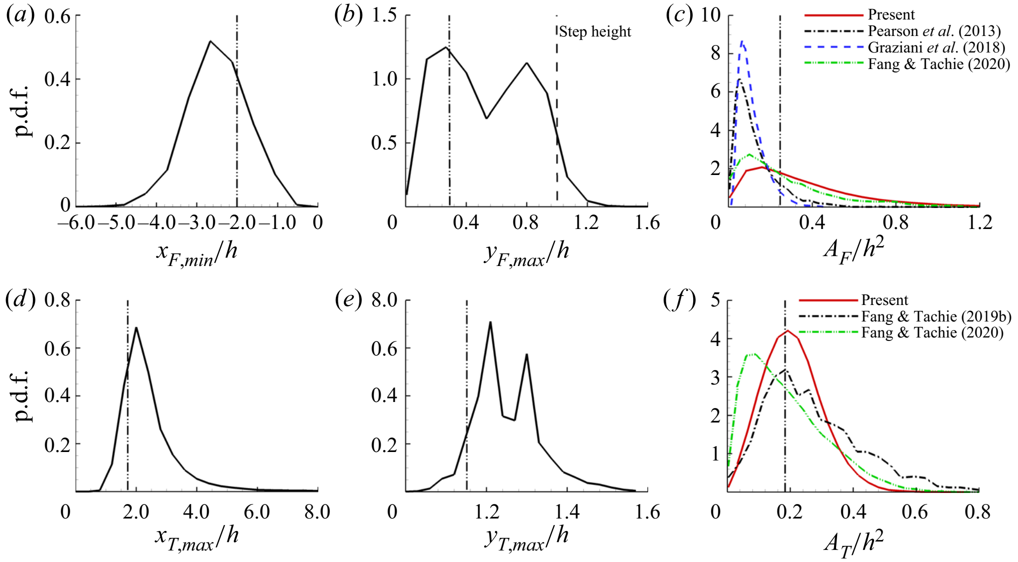

Figure 12. Statistical characterization of reverse flows upstream and downstream of the FFS in the x–y plane. Plots (*a–c*) are the probability density functions (p.d.f.s) of the upstream bound ($x_{F,min}$), upper bound ($y_{F,max}$) and area (A_F) of the reverse flows upstream of the FFS, respectively. Plots (*d–f*) are the p.d.f.s of the downstream bound ($x_{T,max}$), upper bound ($y_{T,max}$) and area (A_T) of the reverse flows on top of the FFS, respectively. The vertical dash-dot-dotted lines mark the values associated with the mean separation bubble. In (*b*) the vertical dashed line marks the step height. Here 25 bins were used to calculate the p.d.f.

using samples extracted from 240 different spanwise grids over 1123 snapshots, which corresponds to 269 520 samples in total. From figures 12(*a*) and 12(*b*), reverse flow upstream of the step can extend far more upstream than the mean separating point on the bottom wall (i.e. $x_{F,min}/h < -2.0$) and spill over the step height (i.e. $y_{F,max}/h > 1.0$). It is interesting to see in figure 12(*b*) that the p.d.f. of $y_{F,max}$ exhibits a bimodal distribution. From figure 4, reverse flows upstream of the step are primarily concentrated in spiky volumes that change elevation abruptly in the spanwise direction. As a consequence, the intermediate values (say $y/h \approx 0.6$) of $y_{F,max}$ are less probable to occur than the mean ($y/h = 0.29$) or excessively high value (say $y/h \approx 0.8$), which manifests as the bimodal distribution of p.d.f.s in figure 12(*b*). As seen in figure 12(*c*), the right tail of the p.d.f. of A_F, which measures the probability of the enlarged separation bubble upstream of the step, is comparable to that in Fang & Tachie (2020), but longer than those in Pearson *et al.* (2013) and Graziani *et al.* (2018). These observations are consistent with conclusions made by Graziani *et al.* (2018) that compared with Pearson *et al.* (2013), their values of A_F were less likely to be extremely large because their step height was higher than the upstream TBL thickness. From figure 4(*d*), the reverse flow over the step can appear downstream of $x/h = 4.0$, which is more than twice of the mean reattachment length. It is observed in figure 12(*e*) that the p.d.f. of the highest elevation of reverse flow over the step ($y_{T,max}$) also exhibits a bimodal distribution. In accordance with figures 12(*c*) and 12(*f*), the present p.d.f. of A_T possesses a shorter right tail than those in Fang & Tachie (2019*b*) and Fang & Tachie (2020) as well as that of the present A_F. This indicates a lower probability of a massive recirculation bubble over the step compared with the recirculation bubble upstream of the step.

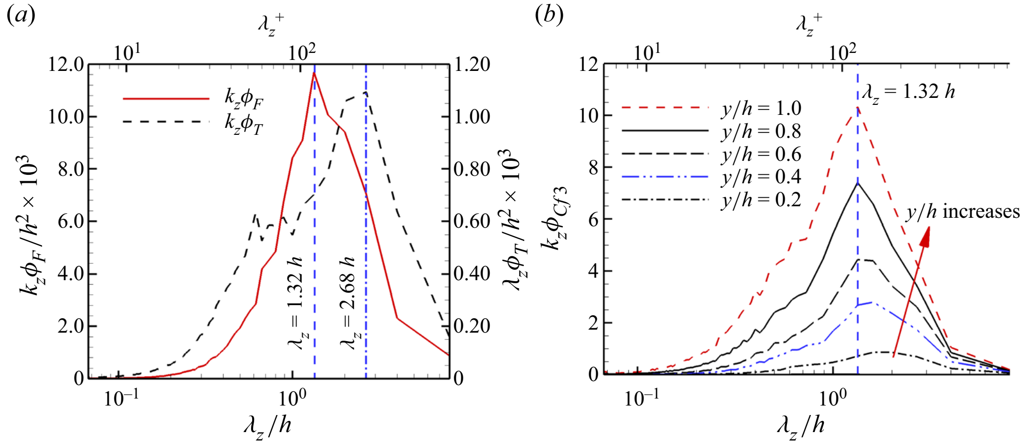

Figure 13. (*a*) Spanwise premultiplied spectra of reverse flow areas upstream (ϕ_F) and downstream (ϕ_T) the step. (*b*) Spanwise premultiplied spectra of C_{f3} (ϕ_{Cf3}) at different elevations on the frontal surface of the step. The arrow marks the monotonic variation as y/h increases. Vertical dashed and dash-dotted lines mark the wavelengths of $\lambda_z/h = 1.32$ and 2.68, respectively.

We now turn attention to the spanwise variation of reverse flows upstream and downstream of the step. Figure 13 characterizes the premultiplied spectra of reverse flow area upstream (A_F) and downstream (A_T) of the step as well as the spanwise skin friction coefficient (C_{f3}) on the frontal surface of the step in terms of spanwise wavelength (λ_z). Notably, A_F and C_{f3} possess an identical sharp peak at $\lambda_z = 1.32h$. It is therefore concluded that the observed quasi-periodic reverse flow upstream of the step and the alternating saddle-nodal pattern in the skin friction on the frontal face observed in figure 4 have the same spanwise periodicity of $1.32h$. It is also observed in figure 13(*a*) that A_T exhibits a relatively broader (compared with A_F) peak at $\lambda_z = 2.68h$. This is reminiscent of the spanwise periodicity of approximately three step heights observed by Stüer *et al.* (1999), Wilhelm *et al.* (2003) and Lanzerstorfer & Kuhlmann (2012) for laminar flows over an FFS.

To investigate the flow characteristics of massive reverse flow upstream of the step, a conditional averaging approach based on the local maximum reverse flow, which specifies an averaging condition that u at the reference point is negative and smaller than u at the two spanwise neighbour points, is employed. The reference point is chosen at $(x/h, y/h) = (-0.1, 1.0)$ so as to capture the spillover of the upstream separation bubble. The x coordinate of the reference point has also been tested at $x/h = -0.2$, and the results were not significantly changed. Note that the reference points are looped over the entire spanwise domain to maximise the sample size. A similar conditional averaging approach was used by Fang & Tachie (2019*b*) using their x–z plane measurement data upstream of a forward-backward-facing step.

From figures 14(*a*) and 14(*b*), the conditionally averaged shape of reverse flow upstream of the step resembles the localized spillover of reverse flows in the instantaneous flow field shown in figure 4. Immediately downstream of the spillover of the upstream reverse flow, the reverse flow over the step is slightly suppressed, as shown by the lower elevation (y/h) of the isosurface below the bundle of streamlines over the step in figure 14(*a*). Based on the conditionally averaged streamlines in figures 14(*a*) and 14(*b*), the incoming fluids in the near-wall region are entrained into the enlarged upstream separation bubble due to spanwise motion, and subsequently spill over the step. This 3-D topology in the streamlines

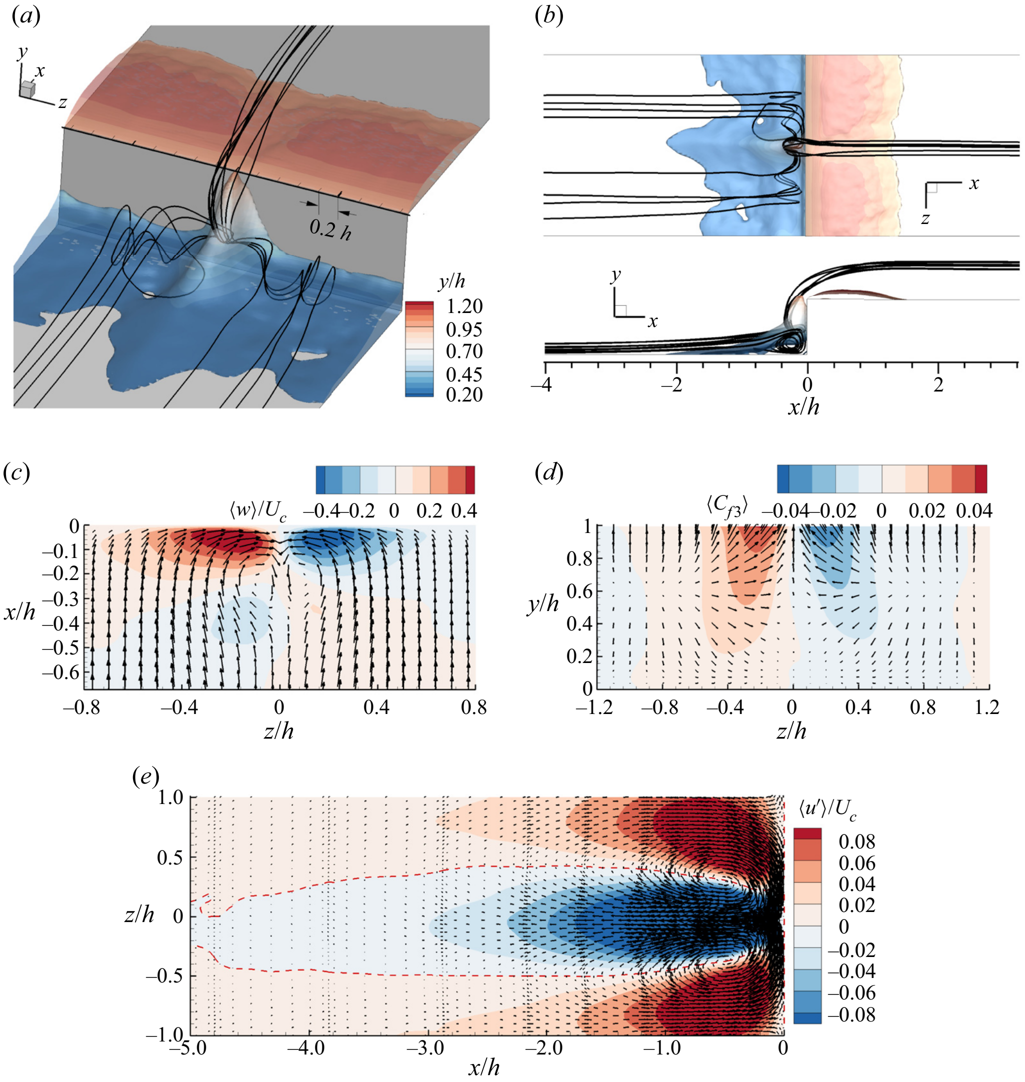

Figure 14. Characterization of conditionally averaged flow field based on the condition of local maximum reverse flow at $(x/h, y/h) = (-0.1, 1.0)$: (*a*,*b*) views of the semi-transparent isosurface of reverse flow and representative streamlines from different perspectives. (*c*) Velocity vectors in the x–z plane at $y/h = 0.8$. (*d*) Skin friction coefficients on the frontal surface of the step. Not all vectors are plotted in (*c*,*d*) for clarity. (*e*) Contour of $\langle u' \rangle$ superimposed with in-plane vectors $(\langle u' \rangle, \langle w' \rangle)$ in the x–z plane at half-step height $(y/h = 0.5)$. The dashed isopleth is $\langle u' \rangle = 0$.

is reminiscent of those observed by Stüer *et al.* (1999) and Wilhelm *et al.* (2003) for an FFS subject to upstream laminar channel flow. In figure 14(*c*) strong spanwise flow motion occurs near the frontal surface $(x/h = 0)$. This is consistent with the excessively high level of $\overline{w'w'}$ observed immediately upstream of the step in figure 7(*g*). From figure 14(*d*), the spillover of upstream reverse flow is associated with positive and negative C_{f3} on the frontal surface on the left and right sides (viewed from the upstream direction), respectively. This is consistent with the observation in figures 13(*a*) and 13(*b*) that the dominant spanwise wavelengths of A_F and C_{f3} are identical.

The conditionally averaged fluctuating velocity vectors $(\langle u'\rangle, \langle w'\rangle)$ in the x–z plane at half-step height $(y/h = 0.5)$ is shown in figure 14(e). From the figure, a pair of counter-rotating vortices flank a distinct low-velocity streamwise-elongated structure extending far (still visible at $x/h = -5.0$) upstream of the step. This pattern of conditionally averaged fluctuating velocity is qualitatively similar to that observed by Fang & Tachie (2019b). The results indicate that an enlarged separation bubble upstream of the step is associated with an incoming low-velocity streaky structure, which conclusion was also made by Pearson *et al.* (2013), Fang & Tachie (2019b) and Fang & Tachie (2020). This conclusion further suggests that the spanwise periodicity of A_F at $1.32h$ (see figure 13a), which corresponds to $119\nu/U_\tau$ in terms of wall units, is a manifestation of the spanwise spacing $(\approx 100\nu/U_\tau)$ between adjacent streaky structures embedded in the oncoming turbulent flow (see figure 3d) (Jiménez & Moin 1991; Flores & Jiménez 2010). Since the low-velocity streaky structure is induced by streamwise aligned hairpin structures, which are commonly termed 'hairpin packets' (Adrian *et al.* 2000), the observation in figure 14(e) prompts us to further study the interaction of an incoming hairpin structure with the FFS.

3.5. *Interaction of an idealized hairpin structure with the FFS*

In this section a modified version of the numerical procedure proposed by Zhou *et al.* (1999) is used to investigate the interaction between an idealized hairpin structure with the FFS. Specifically, DNS (hereinafter denoted as DNS$_h$) was conducted with an initial condition that is a superposition of the turbulent mean flow and the fluctuating velocity field associated with a conditional eddy, which is formulated as

$$u_i(\boldsymbol{X}, t = 0) = \bar{u}_i(\boldsymbol{X}) + \langle u_i'(\boldsymbol{X}) | \boldsymbol{u}'(\boldsymbol{X}_{ref})\rangle = \bar{u}_i(\boldsymbol{X}) + \sum_{j=1}^{3} L_{ij}(\boldsymbol{X}, \boldsymbol{X}_{ref}) u_j'(\boldsymbol{X}_{ref}). \tag{3.8}$$

In the above equation, the LSE (Adrian & Moin 1988) is used to prescribe the optimum approximation of $\langle u_i'(\boldsymbol{X}) | \boldsymbol{u}'(\boldsymbol{X}_{ref})\rangle$. In the framework of LSE, the coefficients $L_{ij}(\boldsymbol{X}, \boldsymbol{X}_{ref})$ at each grid point $(\boldsymbol{X})$ can be calculated by solving a 3×3 linear set of equations defined by

$$\sum_{j=1}^{3} \overline{u_k'(\boldsymbol{X}_{ref}) u_j'(\boldsymbol{X}_{ref})} L_{ij}(\boldsymbol{X}, \boldsymbol{X}_{ref}) = \overline{u_k'(\boldsymbol{X}_{ref}) u_i'(\boldsymbol{X})}. \tag{3.9}$$

Evidently, $L_{ij}(\boldsymbol{X}, \boldsymbol{X}_{ref})$ is only dependent on the unconditional two-point correlations, i.e. $\overline{u_k'(\boldsymbol{X}_{ref}) u_j'(\boldsymbol{X}_{ref})}$ and $\overline{u_k'(\boldsymbol{X}_{ref}) u_i'(\boldsymbol{X})}$. Following Zhou *et al.* (1999), the conditional event is quantified as $(u'_{1,ref}, u'_{2,ref}, u'_{3,ref}) = \alpha(u'_m, v'_m, 0)$, where α is a positive constant defining the event strength, (u'_m, v'_m) represents the ejection event $(u' < 0, v' > 0)$ contributing the most to Reynolds shear stress $\overline{u'v'}$, i.e. the peak of the weighted (using $|u'v'|$) joint p.d.f. of u' and v'.

In Zhou *et al.* (1999), Kim, Sung & Adrian (2008) and Goudar, Breugem & Elsinga (2016), the evolution of the initial conditional eddy was investigated by solving the continuity and N–S equations identical to those used to conduct conventional DNS for the turbulent flows. However, we note that without the correct level of fluctuation velocities to generate the correct values of the Reynolds stresses, the turbulent mean flow cannot sustain itself under the dynamic system prescribed by the N–S equations. In view of this, in the implementation of DNS$_h$, we artificially include the Reynolds stress gradient term in the N–S equation, i.e. the body force term f_i in (2.2) is defined as

$$f_i = -\frac{\partial \overline{u_i' u_j'}}{\partial x_j}. \tag{3.10}$$

As such, in DNS$_h$, the turbulent mean flow remains invariant without any prescribed perturbation, so that the evolution of a single hairpin structure in the background of turbulent mean flow can be studied unambiguously.

The reference point in (3.8) is chosen at $(x/h, y/h, z/h) = (-20.0, 1.0, 0)$ in order to allow a hairpin structure to mature prior impinging onto the FFS. It should be noted that in the initial fluctuating velocity field, the perturbation outside the cuboid box of $x/h \times y/h \times z/h = [-24, -18] \times [0, 2.0] \times [-0.6, 0.6]$ is set to zero. This cuboid box is chosen by a simple visual inspection to contain the dominant features (such as legs and head) of the hairpin structure. In a precursor simulation of DNS$_h$, the residual (low intensity) perturbation prescribed by LSE outside the designated cuboid box is inevitable and can smear the interaction between the incoming hairpin structure and the step (the separation bubbles were altered far before the hairpin structure approaches the step). This indirectly demonstrates the sensitivity of the separation bubbles induced by FFS to the incoming perturbation (Wilhelm *et al.* 2003). The strength (α) of the initial hairpin structure is examined for $\alpha = 0.5$, 1.0, 2.0 and 3.0.

The evolution of the hairpin structure is visualized in figure 15 using isosurfaces of λ_{ci}. In the figure the spanwise elongated isosurfaces identify the vortex cores of two mean separation bubbles upstream and downstream of the step at $tU_C/h = 24.0$. As time increases from $tU_C/h = 0$ to 18.0, the streamwise and vertical extents of the hairpin structure increase. The hairpin structure at $tU_C/h = 18.0$ possesses a 'kink' in the legs. As explained by Zhou *et al.* (1999), this kink is due to the self-induction mechanism of the hairpin legs, and will eventually grow into a new hairpin structure upstream of the primary one. The regeneration mechanism of the hairpin structure has been extensively studied by Acarlar & Smith (1987*a*,*b*), Zhou *et al.* (1999), Kim *et al.* (2008), Goudar *et al.* (2016) and Jodai & Elsinga (2016). In this paper we limit our attention to the interaction between the primary hairpin structure with the FFS.

Figure 16(*a*) shows temporal variation of the reverse flow areas upstream and downstream of the step (A_F and A_T, respectively) at the spanwise centre of the incoming hairpin structure with different initial strengths (α). The values of A_F and A_T remain constant prior to $tU_C/h = 24.0$, when the hairpin structure is not close enough to the step. Indeed, by adding the body force (f_i) prescribed in (3.10) into the N–S equation, the turbulent mean flow is sustained without any imposed perturbation. Therefore, the subsequent variation in separation bubbles is solely due to the effect of the incoming hairpin structure. As seen in figure 16(*a*), A_F increases while A_T decreases for $tU_C/h \in [24.0, 35.0]$. This is consistent with the deduction from figure 11(*a*) that an enlarged separation bubble upstream of the step is typically associated with a contracted separation bubble over the step. Moreover, the temporal variations of A_F and A_T get stronger as the initial strength of the hairpin structure (α) increases. Based on figure 16(*b*–*e*), on the other hand, the topologies of reverse flows and streamlines are qualitatively similar for different values of α, and resemble those observed in figure 14. This provides further support for the earlier observation that the incoming low-velocity streaky structure (at the centre of hairpin structure) enlarges the separation bubble upstream of the step. By comparing figure 16(*b*–*e*), it becomes clear that as the strength of the incoming hairpin structure increases, the separation bubble over the step is increasingly suppressed at the mid-span. With the strongest examined strength ($\alpha = 3.0$), there exists a hole in the isosurface of

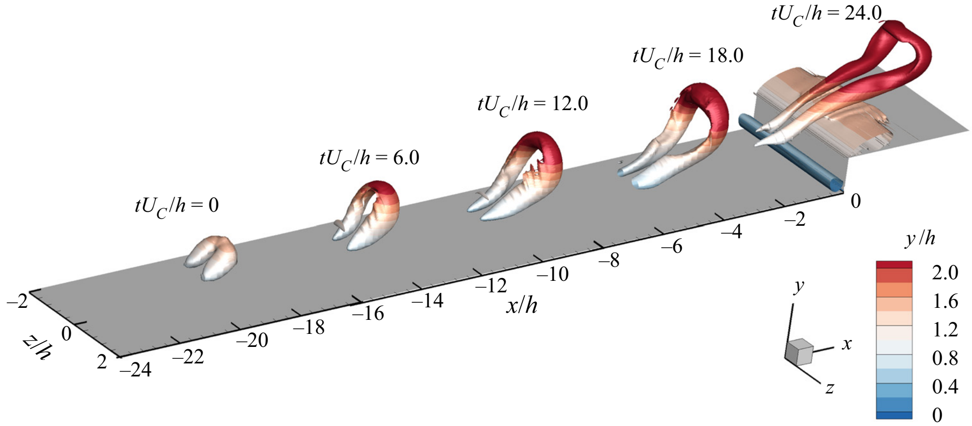

Figure 15. Time evolution of a hairpin structure visualized using the isosurfaces of $\lambda_{ci} = 1.0U_C/h$ from DNS$_h$. The initial hairpin is extracted based on the ejection event at $(x/h, y/h, z/h) = (-20.0, 1.0, 0)$ and the strength α is set to 3.0. The isosurfaces in the upstream corner and immediately downstream of the leading edge are at $tU_C/h = 24.0$.

reverse flow over the step as marked by a dashed circle in figure 16(*e*). This pattern of holes in the isosurface of reverse flow over the step is also visible in the instantaneous flow field (see figures 4(*a*) and 4(*b*), as well as the supplementary animation). This further suggests that the interaction of an idealized hairpin structure with the step can represent generic flow features near an FFS with oncoming turbulent flows, and, therefore, the instantaneous velocity and vorticity fields for figure 16(*e*) are further explored in the subsequent discussion.

Figure 17(*a*) shows the instantaneous flow field at the mid-span for figure 16(*e*). Upstream of the step, the separation bubble is significantly enlarged and the maximum elevation of the reverse flow is around $y/h = 0.8$. This elevation coincides with the second peak location of the p.d.f. of $y_{F,max}$ in figure 12(*b*), indicating that the bimodal distribution of p.d.f.s in figure 12(*b*) reflects the intermittency of the hairpin structure at a fixed spanwise location. The in-plane streamlines upstream of the step do not exhibit a recirculating pattern. This is similar to the 'open-type' streamline associated with a massive separation bubble upstream of the FFS observed by Pearson *et al.* (2013). Over the step, two recirculation bubbles are apparent. This is reminiscent of the separation bubble break-up event observed by Fang & Tachie (2019*b*) over a forward-backward-facing step. Pearson *et al.* (2013) focused their investigation on the separation upstream of the step, while Fang & Tachie (2019*b*) focused only on the separation bubbles over and behind of a forward-backward-facing step. The results shown in figure 17(*a*) indicate that the 'open-type' streamline upstream of the FFS observed by Pearson *et al.* (2013) and the separation bubble break-up event observed by Fang & Tachie (2019*b*) occur concurrently. From figure 17(*b*), a streamwise-elongated volume of negative u' leans over the step, meanwhile positive u' appears in the near-wall region over the step. The superposition between negative u' with mean flow in the upstream corner enlarges the upstream separation bubble, while the positive u' near the top surface of the step reduces the downstream separation bubble. This is consistent with the previous conclusion that the flapping motions of upstream and downstream separation bubbles are out of phase.

To further understand the underlying mechanism of the structure shown in figure 17(*b*), figures 18(*a*) and 18(*b*) examine the fluctuating velocity field in the cross-stream planes

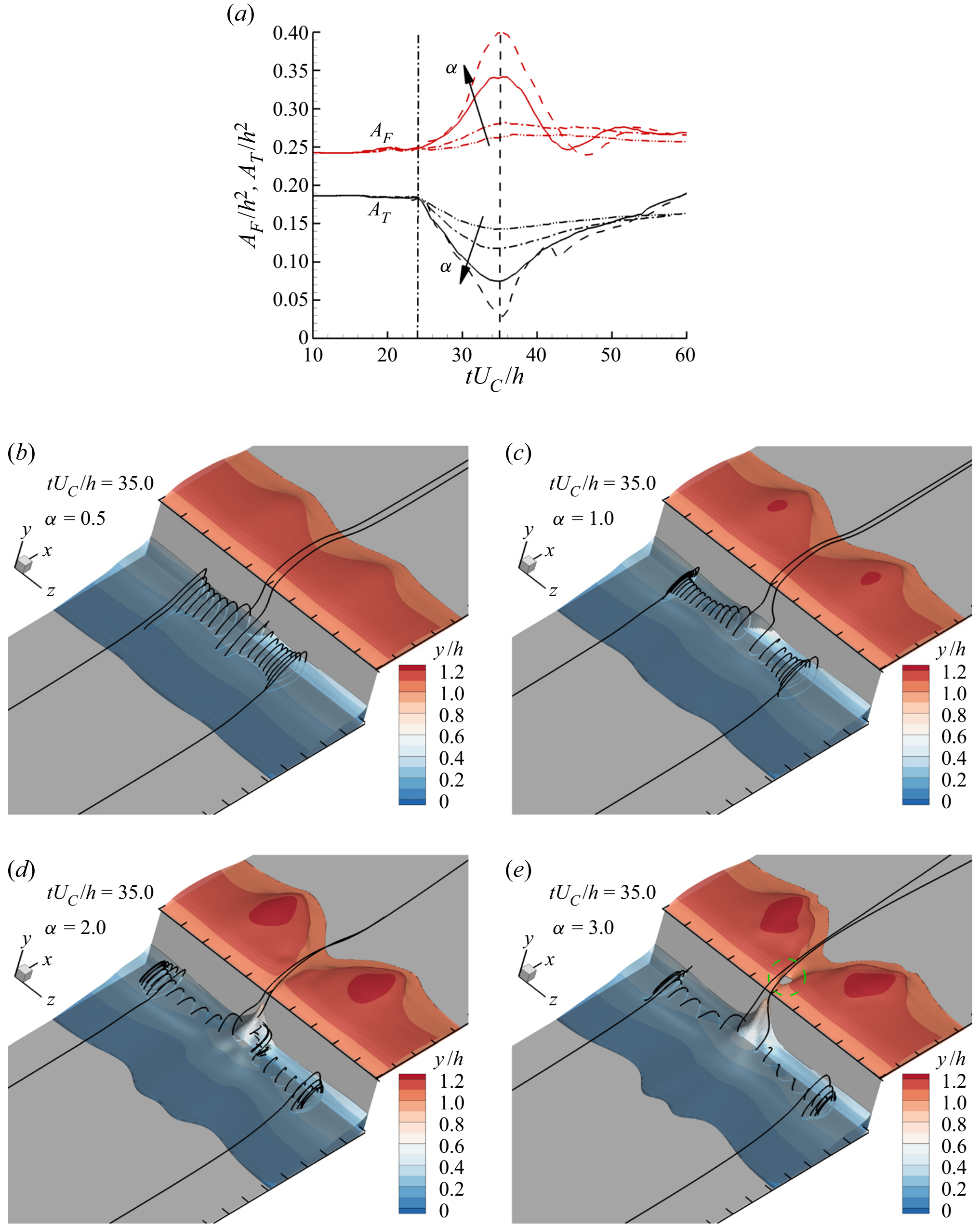

Figure 16. (*a*) Time variation of A_F and A_T at the mid-span with different strengths of initial hairpin structures (α). The arrows mark the monotonic variation of A_F and A_T for $\alpha = 0.5$, 1.0, 2.0 and 3.0. The vertical dash-dotted and dashed lines mark $tU_C/h = 24.0$ and 35.0, respectively. Plots (*b–e*) are the isosurfaces of reverse flows and representative streamlines at $tU_C/h = 35.0$ for $\alpha = 0.5$, 1.0, 2.0 and 3.0, respectively. The distance between adjacent tick marks is $0.4h$. In (*e*) a dashed circle marks a hole in the isosurface of reverse flow over the step.

at $x/h = 0.3$ and 1.6. The former streamwise location is between the dual separation bubbles shown in figure 17(*a*), while the latter is far downstream of the reattachment point over the step, i.e. $x/h = 1.6$. As marked by dashed circles in the figures, two

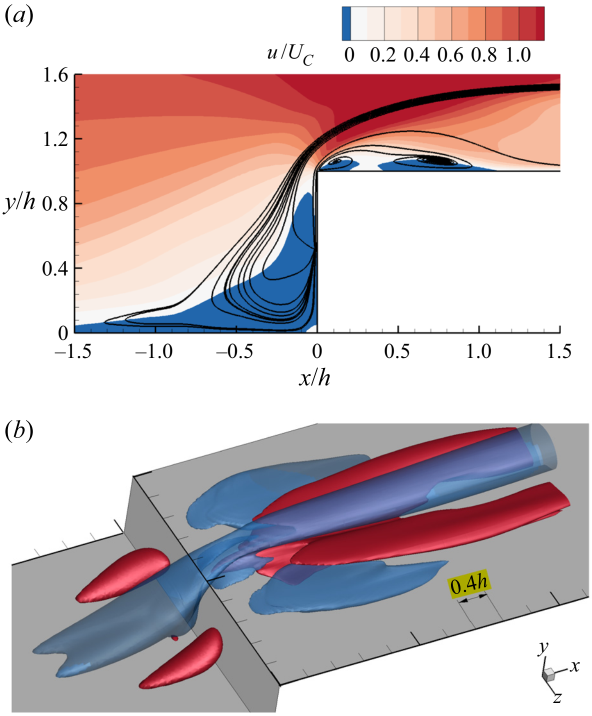

Figure 17. Characterization of the velocity field for figure 16(*e*). (*a*) Contour of streamwise instantaneous velocity u superimposed with in-plane streamlines at the mid-span. (*b*) Isosurfaces of (semi-transparent blue) $u'/U_C = -0.1$ and (solid red) $u'/U_C = 0.1$.

opposite-signed pairs of counter-rotating vortices are apparent. While the hairpin structure is leaning over the step, the hairpin legs manifest as the pair of counter-rotating streamwise vortices at higher elevations in figures 18(*a*) and 18(*b*), and a pair of counter-rotating vertically aligned vortices upstream of the step shown in figure 18(*c*). The occurrence of an opposite-signed pair of counter-rotating vortices at a lower elevation in figures 18(*a*) and 18(*b*) is reminiscent of the induction mechanism to generate opposite-signed secondary vortices in the near-wall region (Acarlar & Smith 1987*b*; Brooke & Hanratty 1993; Bernard, Thomas & Handler 1993; Zhou *et al.* 1999; Dehtyriov, Hourigan & Thompson 2020). The upper pair of counter-rotating vortices generate a Q2 event (i.e. ejection event featuring $u' < 0$ and $v' > 0$) in the centre, whereas the lower pair generates a Q4 event (i.e. sweep event featuring $u' > 0$ and $v' < 0$) in the centre near the top surface of the step. Consequently, the opposite-signed pairs of counter-rotating streamwise vortices induce abrupt switching between Q2 and Q4 events in the centre (see figure 18*d*).

It is remarkable to observe that the pattern of flow structure presented in figure 18 is similar to those revealed using LSE vectors in figure 9(*a*,*c*,*e*). More specifically, both figures 9(*a*) and 18(*d*) show a spanwise vortex around $y/h = 1.2$ above the mean reattachment point over the step. Figure 18(*a*,*b*) shows that the upper pair of counter-rotating vortices does not vary significantly between $x/h = 0.3$ and 1.6. These upper vortices occur around $y/h = 1.4$ and are separated by $\Delta z/h = 0.5$, while those revealed by the LSE vectors in figure 9(*c*) are at a slightly higher elevation (around $y/h = 1.5$) and also separated by $\Delta z/h = 0.5$. By comparing figure 18(*a*,*b*), the pair of counter-rotating vortices in the near-wall region becomes larger in the

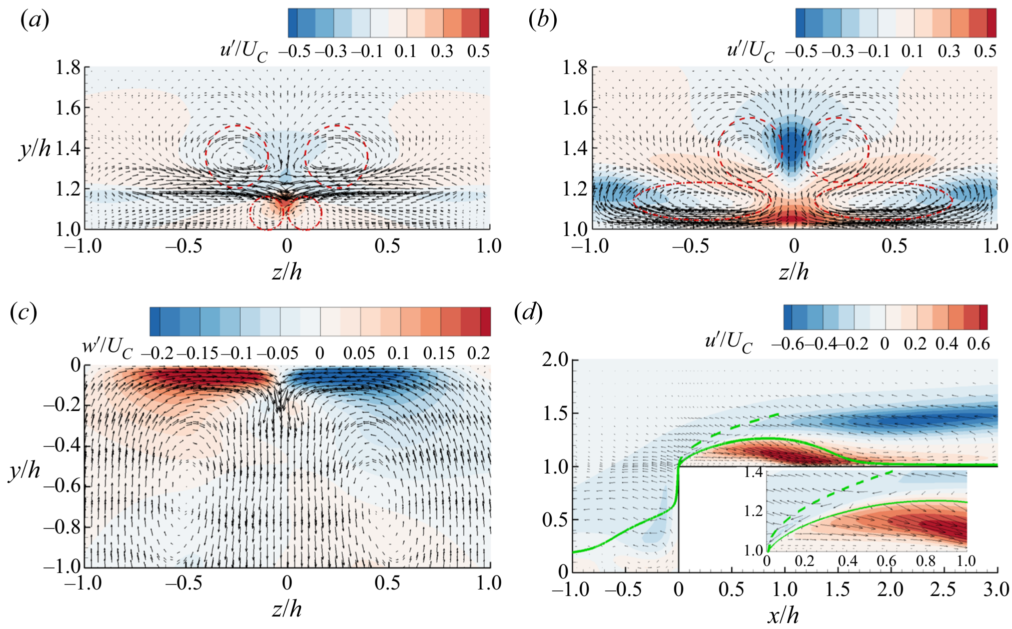

Figure 18. Contours of streamwise fluctuating velocity u' superimposed with vectors (w', v') in the z–y planes at (a) $x/h = 0.3$ and (b) 1.6, respectively. Dashed circles mark two pairs of counter-rotating vortices. (c) Contour of w' superimposed with vectors (w', u') in the z–x plane at $y/h = 0.25$ upstream of the step. (d) Contour of u' at the mid-span superimposed with mean separating streamlines and vectors (u', v'). Not all vectors are shown for clarity. The dashed line represents the location of the PSL.

downstream direction. At $x/h = 0.3$, both figures 9(c) and 18(a) show the pair of counter-rotating vortices in the near-wall region is around $y/h = 1.1$ and are separated by $0.2h$ in the spanwise direction. In the z–x plane at the half-step height ($y/h = 0.5$), both figures 9(e) and 18(c) show a pair of counter-rotating vortices around $x/h = -0.6$ and their spanwise distance is between $0.8h$ and h. These spanwise widths ($0.8h$ and h) correspond to 72–90 wall units, and, thus, are similar to the typical spanwise width of near-wall streaky structures. This is expected due to the fact that streaky structures are generated by streamwise-aligned multiple hairpin structures (Zhou *et al.* 1999). These aforementioned similarities between figures 9 and 18 demonstrate that the interaction between an idealized hairpin structure and the step well represents a salient flow feature over the step with the oncoming fully developed turbulent channel flow.

We further examine the interaction between hairpin structure and the step from the perspective of fluctuating vorticity field. Figure 19 shows the fluctuating vorticity field at the x–y plane crossing one of the hairpin legs (at $z/h = 0.3$). In accordance with figures 18(d) and 19, fluctuating velocity and vorticity both switch directions abruptly near the same location. This agrees with the previous conclusion for figure 18 that the switching between Q2 and Q4 events near the mean separating streamline is due to the opposite-signed pairs of counter-rotating streamwise vortices. According to figures 6(b) and 19, the fluctuating vorticity tends to be parallel to the principal stretching. This is a clear indication that the background principal stretching of mean flow dictates the organization of vortical structure. For example, in the region upstream of the frontal surface of the step, the fluctuating vorticity is in the vertical direction as the principal stretching. This stretched vertical vorticity is accompanied with enhanced

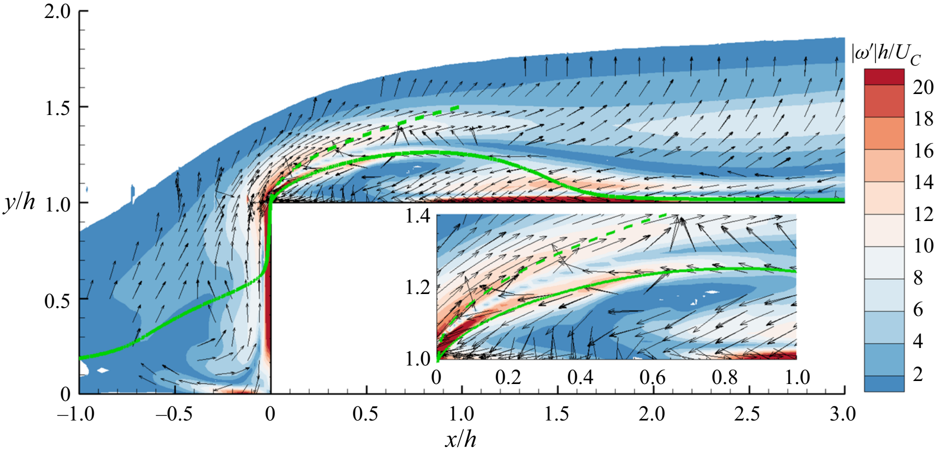

Figure 19. Contour of in-plane fluctuating vorticity magnitude $|\omega'| = (\omega_1'^2 + \omega_2'^2)^{1/2}$ superimposed with vectors $(\omega_1'/|\omega'|, \omega_2'/|\omega'|)$ at $z/h = 0.3$ from DNS$_h$ with the hairpin structure initialized as in figure 15. Note that the area of $|\omega'|h/U_C < 1.4$ is removed to facilitate comparison. Not all vectors are plotted for clarity. The dashed line represents the location of the PSL. The inset magnifies the region near the leading edge over the step.

counter-rotating vortices flanking the low-velocity streaky structure in the z–x plane (see figures 9*e* and 14*e*), and can also generate strong spanwise fluctuating velocity (see figure 7*g*) and skin friction (see figure 5) near/on the frontal surface of the step. It is interesting to see in figure 19 that fluctuating vorticity indeed switches the orientation abruptly along the PSL. In other words, the PSL prevents the vortical structure in oncoming flow from directly interacting with the separation bubble over the step. In spite of a similar PSL observed in our previous experimental study (Fang & Tachie 2020), because of the weak vorticity associated with the uniform momentum zone in the LSM, which is populated in the incoming TBL, the LSM is not strongly affected by the PSL, so that the LSM enlarges/suppresses the separation bubbles upstream of and over the step together. Therefore, the positive R_{FT} observed in Fang & Tachie (2020) and the negative R_{FT} observed in the present DNS study (see figure 11) simply reflects the fact that the LSM does not exist at low Reynolds numbers. Moreover, as has been commented for figure 17(*a*), the separation bubble break-up event observed in Fang & Tachie (2019*b*) is attributed to interaction of incoming hairpin structures with the step. Fang & Tachie (2019*b*) noted that the separation bubble break-up event occurs at a frequency higher than the characteristic frequency of the LSM in the incoming TBL. This is simply because multiple hairpin structures exist in a single LSM.

Thus far, it is clear that the deformation of the hairpin legs by the step alters the separation bubbles upstream of and over the step. Muralidhar *et al.* (2019) showed that in a turbulent channel flow the dominant frequencies signify vortical structures in the cross-stream plane that are convected downstream and feature streamwise-elongated streaky structures. Thus, the observation from figure 10 that the dominant frequencies of the separation bubbles mirror the dominant frequencies of the incoming flow reflects the interaction between incoming streamwise vortical structures and the step.

4. Conclusions

Separating and reattaching turbulent flows induced by a FFS immersed in a fully developed turbulent plane channel flow were systematically investigated using DNS based on the spectral-element-Fourier algorithm. The topological characteristics of principal stretching in the vicinity of the step were examined through an eigendecomposition of the mean strain rate tensor. Statistics of fluctuating velocity and vorticity were analysed with special attention to the effects of mean streamline curvature and spatial variation of principal stretching. Based on the volumes of reverse flow upstream of and over the step, 3-D spatio-temporal unsteady characteristics of the separation bubbles induced by the step were systematically elucidated. The interaction between the oncoming hairpin structure and separation bubbles induced by the step was also studied in detail.

Principal stretching is in the vertical direction near the frontal surface of the step, and is close to parallel to mean streamlines immediately upstream of the leading edge of the step. Over the step, the orientation of principal stretching changes abruptly along a curved line initiated from the leading edge of the step. This curved line is hereinafter denoted by PSL for conciseness. The PSL acts as a ‘shield’ to prevent the vortical structure in oncoming turbulent flow from directly interacting with the near-wall region over the step. In particular, the PSL bounds the areas of elevated Reynolds stresses and second-order moments of fluctuating vorticity components over the step. Immediately upstream of the leading edge of the step, strong fluctuating vorticity parallel to the mean streamline occurs, and is accompanied by a significant fluctuating velocity component perpendicular to the mean streamline and in the spanwise direction. On the frontal surface of the step, strong spanwise friction occurs in the form of alternating positive and negative vertical strips in the spanwise direction.

Separation bubbles upstream of and over the step possess similar dominant and harmonic frequencies, that mirror those frequencies in the incoming flow. The upstream and downstream separation bubbles are generally opposite in phase, i.e. an enlarged upstream separation bubble is typically associated with a contracted downstream separation bubble. This opposite-phased interaction between separation bubbles upstream of and over the step occurs at the dominant and harmonic frequencies similar to those observed in the incoming flow.

As a hairpin structure approaches the step from the upstream location, the hairpin legs (in the form of counter-rotating vortices) are deformed by being stretched by the mean strain. The deformed hairpin structure imposes the maximum influence on the separation bubbles as the accompanied vorticity becomes nearly parallel with the principal stretching. Consequently, a pair of counter-rotating vortices are aligned in the vertical direction near the frontal surface of the step. This further generates strong ejection events which act to enlarge the separation bubble upstream of the step, and also leads to a pair of positive and negative vertically extended strips of spanwise skin friction on the frontal surface of the step. The PSL marks the lower bound of the deformed hairpin legs, and an opposite-signed pair of counter-rotating quasi-streamwise vortices is inducted near the top surface of the step. As a result, the ejection event imposed by the incoming hairpin structure switches to the sweep event along the PSL. This sweep event suppresses the separation bubble over the step. For a sufficiently strong oncoming hairpin structure interacting with the step, dual separation bubbles appear in the central plane over the step, while the separation bubble upstream of the step exhibits an open-type topology.

Supplementary movie. Supplementary movie is available at https://doi.org/10.1017/jfm.2021.395.

Acknowledgements. The computation time and hard drive storage provided by the University of Manitoba are appreciated. We also sincerely thank Blackburn & Sherwin (2004) for generously releasing their spectral-element-Fourier source code (https://users.monash.edu.au/~bburn/semtex.html).

Funding. The financial support from Natural Sciences and Engineering Research Council of Canada (NSERC), [RGPIN-2017-04957] to M.F.T. is gratefully acknowledged.

Declaration of interests. The authors report no conflict of interest.

Author ORCIDs.
Xingjun Fang https://orcid.org/0000-0003-2005-7269;
Mark F. Tachie https://orcid.org/0000-0002-0385-1391;
Zixuan Yang https://orcid.org/0000-0002-7764-3595;
Bing-Chen Wang https://orcid.org/0000-0003-0883-4897.

REFERENCES

ABU-MULAWEH, H.I., ARMALY, B.F. & CHEN, T.S. 1996 Laminar nature convection flow over a vertical forward-facing step. *J. Thermophys. Heat Transfer* **10** (3), 517–523.

ACARLAR, M.S. & SMITH, C.R. 1987*a* A study of hairpin vortices in a laminar boundary layer. Part 1. hairpin vortices generated by a hemisphere proturberance. *J. Fluid Mech.* **175**, 1–41.

ACARLAR, M.S. & SMITH, C.R. 1987*b* A study of hairpin vortices in a laminar boundary layer. Part 2. hairpin vortices generated by fluid injection. *J. Fluid Mech.* **175**, 43–83.

ADDAD, Y., LAURENCE, D., TALOTTE, C. & JACOB, M.C. 2003 Large eddy simulation of forward-backward facing step for acoustic source identification. *Intl J. Heat Fluid Flow* **24**, 562–571.

ADRIAN, R.J., MEINHART, C.D. & TOMKINS, C.D. 2000 Vortex organization in the outer region of the turbulent boundary layer. *J. Fluid Mech.* **422**, 1–54.

ADRIAN, R.J. & MOIN, P. 1988 Stochastic estimation of organized turbulent structure: homogeneous shear flow. *J. Fluid Mech.* **190**, 531–559.

ALAM, M. & SANDHAM, N.D. 2000 Direct numerical simulation of 'short' laminar separation bubbles with turbulent reattachment. *J. Fluid Mech.* **410**, 1–28.

BERNARD, P.S., THOMAS, J.M. & HANDLER, R.A. 1993 Vortex dynamics and the production of Reynolds stress. *J. Fluid Mech.* **253**, 385–419.

BLACKBURN, H.M., LEE, D., ALBRECHT, T. & SINGH, J. 2019 Semtex: a spectral element-Fourier solver for the incompressible Navier–Stokes equations in cylindrical or Cartesian coordinates. *Comput. Phys. Commun.* **245**, 106804.

BLACKBURN, H.M. & SHERWIN, S.J. 2004 Formulation of a Galerkin spectral element-Fourier method for three-dimensional incompressible flows in cylindrical geometries. *J. Comput. Phys.* **197** (2), 759–778.

BROOKE, J.W. & HANRATTY, T.J. 1993 Origin of turbulence-producing eddies in a channel flow. *Phys. Fluids* **5** (4), 1011–1022.

CAMUSSI, R., FELLI, M., PEREIRA, F., ALOISIO, G. & DI MARCO, A. 2008 Statistical properties of wall pressure fluctuations over a forward-facing step. *Phys. Fluids* **20**, 075113.

CHIBA, K., ISHIDA, R. & NAKAMURA, K. 1995 Mechanism for entry flow instability through a forward-facing step channel. *J. Non-Newtonian Fluid Mech.* **57**, 271–282.

DEHTYRIOV, D., HOURIGAN, K. & THOMPSON, M.C. 2020 Direct numerical simulation of a counter-roating vortex pair interacting with a wall. *J. Fluid Mech.* **884**, A36.

DIANAT, M. & CASTRO, I.P. 1984 Fluctuating surface shear stresses on bluff bodies. *J. Wind Engng Ind. Aerodyn.* **17**, 133–146.

DJILALI, N. & GARTSHORE, I.S. 1991 Turbulent flow around a bluff rectangular plate. Part I: experimental investigation. *Trans. ASME: J. Fluids Engng* **113** (1), 51–59.

EATON, J.K. & JOHNSTON, J.P. 1982 Low frequency unsteadiness of a reattaching turbulent shear layer. In *Turbulent Shear Flows* (ed. L.J.S. Bradbury *et al.*), vol. 3, pp. 162–170. Springer.

FANG, X. 2017 The influences of V-shaped ribs and spanwise system rotation on a turbulent square duct flow. Ph.D. thesis, University of Manitoba, Department of Mechanical Engineering.

FANG, X. & TACHIE, M.F. 2019*a* Flows over surface-mounted bluff bodies with different spanwise widths submerged in a deep turbulent boundary layer. *J. Fluid Mech.* **877**, 717–758.

FANG, X. & TACHIE, M.F. 2019*b* On the unsteady characteristics of turbulent separations over a forward-backward-facing step. *J. Fluid Mech.* **863**, 994–1030.

Fang, X. & Tachie, M.F. 2020 Spatio-temporal dynamics of flow separation induced by a forward-facing step submerged in a thick turbulent boundary layer. *J. Fluid Mech.* **892**, A40.

Fang, X., Tachie, M.F. & Bergstrom, D.J. 2021 Direct numerical simulation of turbulent flow separation induced by a forward-facing step. *Intl J. Heat Fluid Flow* **87**, 108753.

Flores, O. & Jiménez, J. 2010 Hierachy of minimal flow units in the logarithmic layer. *Phys. Fluids* **22**, 071704.

Ganapathisubramani, B., Clemens, N.T. & Dolling, D.S. 2007 Effects of upstream boundary layer on the unsteadiness of shock-induced separation. *J. Fluid Mech.* **585**, 369–394.

Goudar, M.V., Breugem, W. -P. & Elsinga, G.E. 2016 Auto-generation in wall turbulence by the interaction of weak eddies. *Phys. Fluids* **28**, 035111.

Graziani, A., Kerhervé, F., Martinuzzi, R.J. & Keirsbulck, L. 2018 Dynamics of the recirculating areas of a forward-facing step. *Exp. Fluids* **59**, 154.

Hattori, H. & Nagano, Y. 2010 Investigation of turbulent boundary layer over forward-facing step via direct numerical simulation. *Intl J. Heat Fluid Flow* **31** (3), 284–294.

Hudy, L.M., Naguib, A.M. & Humphreys, W.M. 2003 Wall-pressure-array measurements beneath a separating/reattaching flow region. *Phys. Fluids* **15** (3), 706–717.

Humble, R.A., Scarano, F. & Van Oudheusden, B.W. 2009 Unsteady aspects of an incident shock wave/turbulent boundary layer interaction. *J. Fluid Mech.* **635**, 47–74.

Jiménez, J. & Moin, P. 1991 The minimal flow unit in near-wall turbulence. *J. Fluid Mech.* **225**, 213–240.

Jodai, Y. & Elsinga, G.E. 2016 Experimental observation of hairpin auto-generation events in a turbulent boundary layer. *J. Fluid Mech.* **795**, 611–633.

Karniadakis, G.E., Israeli, M. & Orszag, S.A. 1991 High-order splitting methods for the incompressible Navier–Stokes equations. *J. Comput. Phys.* **97** (2), 414–443.

Kevin, M.J. & Hutchins, N. 2019 Turbulent structures in a statistically three-dimensional boundary layer. *J. Fluid Mech.* **859**, 543–565.

Kim, K., Sung, H.J. & Adrian, R.J. 2008 Effects of background noise on generating coherent packets of hairpin vortices. *Phys. Fluids* **20**, 105107.

Kim, K.C., Ji, H.S. & Seong, S.H. 2003 Flow structure around a 3-D rectangular prism in a turbulent boundary layer. *J. Wind Engng Ind. Aerodyn.* **91**, 653–669.

Kiya, M. & Sasaki, K. 1983 Structure of a turbulent separation bubble. *J. Fluid Mech.* **137**, 83–113.

Lanzerstorfer, D. & Kuhlmann, H.C. 2012 Three-dimensional instability of the flow over a forward-facing step. *J. Fluid Mech.* **695**, 390–404.

Marino, L. & Luchini, P. 2009 Adjoint analysis of the flow over a forward-facing step. *Theor. Comput. Fluid Dyn.* **23**, 37–54.

Martinuzzi, R. & Tropea, C. 1993 The flow around surface-mounted, prismatic obstacles placed in a fully developed channel flow. *Trans. ASME: J. Fluids Engng* **115**, 85–92.

Mohammed-Taifour, A. & Weiss, J. 2016 Unsteadiness in a large turbulent separation bubble. *J. Fluid Mech.* **799**, 383–412.

Moser, R.D., Kim, J. & Mansour, N.N. 1999 Direct numerical simulation of turbulent channel flow up to $Re_\tau = 590$. *Phys. Fluids* **11** (4), 943–945.

Moss, W.D. & Baker, S. 1980 Re-circulating flows associated with two-dimensional steps. *Aeronaut. Q.* **31** (3), 151–172.

Muralidhar, S.D., Podvin, B., Mathelin, L. & Fraigneau, Y. 2019 Spatial-temporal proper orthogonal decomposition of turbulent channel flow. *J. Fluid Mech.* **864**, 614–639.

Pearson, D.S., Goulart, P.J. & Ganapathisubramani, B. 2013 Turbulent separation upstream of a forward-facing step. *J. Fluid Mech.* **724**, 284–304.

Ren, H. & Wu, Y. 2011 Turbulent boundary layers over smooth and rough forward-facing steps. *Phys. Fluids* **23**, 045102.

Schröder, A., Willert, C., Schanz, D., Geisler, R., Jahn, T., Gallas, Q. & Leclaire, B. 2020 The flow around a surface mounted cube: a characterization by time-resolved PIV, 3D Shake-The-Box and LBM simulation. *Exp. Fluids* **61**, 189.

Sherry, M., Lo Jacono, D. & Sheridan, J. 2010 An experimental investigation of the recirculation zone formed downstream of a forward facing step. *J. Wind Engng Ind. Aerodyn.* **98** (12), 888–894.

Stüer, H., Gyr, A. & Kinzelbach, W. 1999 Laminar separation on a forward facing step. *Eur. J. Mech. B/Fluids* **18**, 675–692.

Tafti, D.K. & Vanka, S.P. 1991 A three-dimensional numerical study of flow separation and reattachment on a blunt plate. *Phys. Fluids* A **3**, 2887–2909.

Thacker, A., Aubrun, S., Leroy, A. & Devinant, P. 2013 Experimental characterization of flow unsteadiness in the centerline plane of an Ahmed body rear slant. *Exp. Fluids* **54**, 1479.

WILHELM, D., HÄRTEL, C. & KLEISER, L. 2003 Computational analysis of the two-dimensional-three-dimensional transition in forward-facing step flow. *J. Fluid Mech.* **489**, 1–27.

YANG, Z. & VOKE, P.R. 2001 Large-eddy simulation of boundary-layer separation and transition at a change of surface curvature. *J. Fluid Mech.* **439**, 305–333.

ZHOU, J., ADRIAN, R.J., BALACHANDAR, S. & KENDALL, T.M. 1999 Mechanisms for generating coherent packets of hairpin vortices in channel flow. *J. Fluid Mech.* **387**, 353–396.